

1 High-Complexity Barcoded Rabies Virus for Scalable Circuit Mapping Using Single-Cell and Single- 2 Nucleus Sequencing

3
4 David Shin^{1,2,12}, Madeleine E. Urbanek^{1,2,12}, H. Hanh Larson², Anthony J. Moussa³, Kevin Y. Lee², Donovan L.
5 Baker², Elio Standen-Bloom², Sangeetha Ramachandran^{1,2}, Derek Bogdanoff⁴, Cathryn R. Cadwell^{2,5,6,7,8,13*},
6 Tomasz J. Nowakowski^{2,7,9,10,11,13,14**}

7
8 ¹Biomedical Sciences Graduate Program, University of California, San Francisco, CA, USA

9 ²Department of Neurological Surgery, University of California, San Francisco, CA, USA

10 ³Medical Scientist Training Program, University of California, San Francisco, CA, USA

11 ⁴Tetrad Graduate Program, University of California, San Francisco, CA, USA

12 ⁵Department of Pathology, University of California, San Francisco, CA, USA

13 ⁶Weill Neurohub, University of California, San Francisco, CA, USA

14 ⁷Weill Institute for Neurosciences, University of California, San Francisco, CA, USA

15 ⁸Kavli Institute for Fundamental Neuroscience, University of California, San Francisco, CA, USA

16 ⁹Department of Anatomy, University of California, San Francisco, CA, USA

17 ¹⁰Department of Psychiatry and Behavioral Sciences, University of California, San Francisco, CA, USA

18 ¹¹Eli and Edythe Broad Center for Regeneration Medicine and Stem Cell Research, University of California,
19 San Francisco, CA, USA

20 ¹²These authors contributed equally

21 ¹³Senior author

22 ¹⁴Lead contact

23 *Correspondence: Cathryn.Cadwell@ucsf.edu

24 **Correspondence: Tomasz.Nowakowski@ucsf.edu

25 **SUMMARY**

26 Single cell genomics has revolutionized our understanding of neuronal cell types. However, scalable
27 technologies for probing single-cell connectivity are lacking, and we are just beginning to understand how
28 molecularly defined cell types are organized into functional circuits. Here, we describe a protocol to generate
29 high-complexity barcoded rabies virus (RV) for scalable circuit mapping from tens of thousands of individual
30 starter cells in parallel. In addition, we introduce a strategy for targeting RV-encoded barcode transcripts to the
31 nucleus so that they can be read out using single-nucleus RNA sequencing (snRNA-seq). We apply this tool in
32 organotypic slice cultures of the developing human cerebral cortex, which reveals the emergence of cell type–
33 specific circuit motifs in midgestation. By leveraging the power and throughput of single cell genomics for
34 mapping synaptic connectivity, we chart a path forward for scalable circuit mapping of molecularly-defined cell
35 types in healthy and disease states.

36

37 **KEYWORDS**

38 Barcoded rabies virus, single-cell RNA sequencing, single-nucleus RNA sequencing, human, brain
39 development, cortex, subplate, barcode complexity, barcode diversity

40

41 INTRODUCTION

42 Understanding neuronal connectivity at the cell type level is crucial for unraveling the complexities of brain
43 function and dysfunction. Monosynaptic tracing using glycoprotein (G)-deleted rabies virus (RVdG) has been a
44 powerful method for mapping direct synaptic connections between populations of cells^{1,2}. This method exploits
45 the natural ability of RVdG to spread trans-synaptically in the retrograde direction, allowing researchers to
46 trace connections from a genetically targeted starter cell population to its presynaptic partners. Despite its
47 utility, traditional monosynaptic rabies tracing methods have limitations. For example, these techniques
48 typically offer only coarse cell-type specificity due to the limitations of transgenic mouse lines and viral tools
49 used for targeting specific cell populations. With the advent of single-cell RNA sequencing, the neuronal
50 landscape has been shown to be much more complex, revealing a multitude of fine-grained cell types that
51 cannot be distinguished with existing tracing methods.

52 Several recent studies have incorporated a nucleotide 'barcode' into the RVdG backbone, enabling
53 simultaneous readout of the connectivity and cell identity of hundreds of cells in a single experiment using
54 single cell or spatial transcriptomics assays³⁻⁵. However, this barcoded RVdG technology still faces significant
55 challenges. First, in contrast to other viruses such as lentivirus or adeno-associated virus, it has been
56 challenging to achieve high-complexity libraries of barcoded RVdG, and the limited diversity of barcoded RVdG
57 libraries represents a major roadblock to scaling this technology to study larger networks. There are multiple
58 reasons for this, including the low efficiency of active viral RNA particle recovery from a DNA template and
59 variable clonal expansion of the few barcodes that are recovered, among others⁶⁻⁸. Second, given that RVdG
60 replicates and undergoes transcription in the cytoplasm^{9,10}, it has not been possible to read out RVdG
61 barcodes from isolated nuclei, necessitating whole cell dissociations which compromise neuron viability and
62 integrity, further limiting the utility of this tool.

63 To overcome these challenges, we have developed an optimized protocol for RVdG packaging to
64 improve the complexity of barcoded RVdG libraries by several orders of magnitude compared to currently
65 published tools. This advancement significantly enhances the scalability of trans-synaptic tracing experiments,
66 allowing us to potentially map the inputs to tens of thousands of single cells in parallel. Additionally, we have
67 incorporated a method for localizing RVdG barcodes to nuclei, allowing for high-fidelity connectivity mapping

68 without the need for whole cell dissociations. To demonstrate the power of this tool, we characterize the
69 emergence of cell type–specific connectivity patterns by mapping the inputs to thousands of single starter cells
70 in organotypic slices of the developing human cerebral cortex.

72 RESULTS

74 **Generation of high-complexity barcoded RVdG libraries enables mapping the inputs to thousands of** 75 **single cells in parallel**

76 To generate a high-complexity barcoded RVdG plasmid library, we have leveraged a recently developed
77 combinatorial barcode system optimized for scRNA-seq readout¹¹. This barcode ‘white list’ system generates
78 barcode complexity exponentially using combinatorial indexing, while maintaining a high (≥ 6) minimum
79 Hamming distance that is robust to sequencing errors ([Figures S1A and S1B; Table S1](#)). We cloned these
80 barcodes into the 3' UTR of the fourth open reading frame of the RVdG genome plasmid encoding dTomato
81 ([Figures 1A, 1B, S1C and S1D; Table S2](#)).

82 We optimized a protocol for packaging RVdG to improve barcode complexity and promote a more
83 uniform distribution of viral barcodes ([Figure 1C–1G and Figure 2](#)). Using this optimized RVdG packaging
84 protocol, we were able to generate high-complexity barcoded RVdG libraries which contained millions of
85 unique barcodes with a relatively even barcode distribution compared to prior published libraries^{3–5} (GEO:
86 GSE277536). Specifically, no single barcode in our packaged RVdG libraries accounts for more than 0.046%
87 of the total number of barcodes detected ([Figure 1D](#)). In order to estimate the number of unique starter
88 infections that can be traced using different barcoded RVdG libraries, we used a simulation to compute the rate
89 of barcode collision, or at least two starter cells receiving the same barcode, as a function of the number of
90 cells infected. This simulation revealed that our optimized RVdG libraries enable unique labeling of 10,000 to
91 100,000 single cells with a barcode collision rate less than 10%, which represents two to three orders of
92 magnitude improvement compared to previously published libraries ([Figure 1E](#)). This increased barcode
93 complexity of our libraries persisted across a broad range of simulated sequencing depths ([Figure 1F](#)). We

94 also quantified the complexity of our barcoded RVdG libraries using an estimate of Shannon entropy^{12,13} and
95 found that our optimized libraries correspond to an approximately 8-bit improvement in information content
96 compared to previously published libraries ([Figure 1G](#)). A difference in a single bit represents a doubling of
97 library complexity through increasing either the number of barcodes, uniformity of the barcode distribution, or
98 both ([STAR Methods](#)). In summary, our optimized RVdG packaging protocol leads to a robust improvement in
99 barcoded RVdG library complexity compared to prior studies.

101 **The HEK-GT cell line and Lipofectamine 3000 transfection reagent are optimal for generating high-** 102 **complexity barcoded RVdG libraries**

103 Current state-of-the-art protocols for packaging RVdG involve a three-step process^{4,6,14,15}: First, a packaging
104 cell line (e.g. HEK293T, Neuro2A, or B7GG cells) undergoes transfection with packaging plasmids, which
105 include an RVdG genome plasmid, four plasmids encoding RV proteins (N, P, L, and G) necessary for RVdG
106 packaging and propagation, and a plasmid encoding T7 polymerase to drive the expression of the RVdG
107 genome. The initial recovery of replication-competent viral particles from plasmid DNA at this step is extremely
108 inefficient, with some reports suggesting that less than 0.01% of transfected cells successfully begin to
109 produce RVdG^{4,16}. As a result, in the second step RVdG is given time to propagate throughout the culture until
110 a majority of cells are producing the virus ([Figure S1E](#)). Third, G-pseudotyped viral supernatant is harvested
111 and used to transduce BHK21 cells that stably express EnvA in order to produce EnvA-pseudotyped RVdG
112 ([Figure S1F](#)), which is subsequently collected and concentrated by ultracentrifugation and used for
113 downstream experiments.

114 We reasoned that improving the efficiency of recovering viral particles from plasmid DNA might improve
115 the diversity and distribution of our barcoded RVdG viral libraries ([Figure 2A](#)). We evaluated the efficiency of
116 commonly used cell lines for packaging RVdG: HEK293T, BHK-21, and Neuro2A ([Figures 2B, S1G–S1J](#)). We
117 transfected each cell line with packaging plasmids in the absence of rabies G to disable cell-to-cell viral
118 spread, and quantified the percentage of cells that rescued RVdG using flow cytometry. HEK293T cells were
119 more efficient at packaging RVdG, rescuing RVdG at rates approximately 48-fold higher than BHK-21 cells and
120 ~29-fold higher than Neuro2A cells (HEK293T: 0.32±0.13%, BHK21: 0.0067±0.0027%, Neuro2A: 0.011±

0.0045%, mean \pm SEM; HEK293T vs. BHK21: $p=0.013$, HEK293T vs. Neuro2A: $p=0.013$, BHK21 vs. Neuro2A: $p=0.53$, Wilcoxon rank sum test with Bonferroni-Holm correction for family-wise error rate; [Figures 2B, S1G–S1J](#)).

We also tested different transfection reagents to identify those that might further improve viral rescue efficiency in HEK293T cells ([Figures 2C, S1I, and S1J](#)). Lipofectamine 3000 (Lipo3000) and PEI MAX showed the highest efficiencies of viral rescue (Lipo3000: $0.38\pm 0.05\%$; PEI MAX: $0.37\pm 0.05\%$). These reagents yielded a 2.9-fold improvement in viral rescue on average compared to Lipofectamine 2000 (Lipo2000) and a 5.8-fold improvement compared to Xfect, two transfection reagents previously used for barcoded RVdG packaging^{3–5} ([Figures 2C, S1I, and S1J](#)).

We next prepared barcoded viral libraries to directly compare the diversity achieved using Lipo3000 and Lipo2000 ([STAR Methods](#)) in HEK293T cells. RVdG prepared with Lipo3000 exhibited a more even barcode distribution compared to Lipo2000, with the most common barcode in Lipo3000 libraries accounting for on average 0.18% of total barcoded genomes detected, compared to 2.84% in Lipo2000 libraries ([Figure 2D](#)). The rate of barcode collision was lower, and the Shannon entropy was higher, in Lipo3000 compared to Lipo2000 libraries ([Figures S1K and S1L; STAR Methods](#)).

We reasoned that some barcoded RVdG particles might gain a competitive advantage during viral propagation due to variability in rabies G expression, leading to overrepresentation of a subset of barcodes. To test this, we leveraged a recently developed packaging cell line, HEK-GT, which is a HEK293T cell line that stably expresses the chimeric rabies glycoprotein oG and T7 polymerase^{17,18} ([Figure 2E](#)). Indeed, HEK-GT cells produced RVdG libraries with a more uniform barcode distribution compared to HEK293T ([Figures 2F, S1K, and S1L](#)). Another proposed solution for uneven viral propagation during packaging is to physically constrain the amplification of barcoded RV clones by using multi-well plates with a smaller surface area¹⁹. However, we found no difference in library complexity between barcoded RV libraries packaged in 15 cm dishes and 384-well plates ([Figures S1M–S1N](#)).

Helper virus– and RVdG–infected cells are predominantly neuronal in human prenatal organotypic slice cultures

148 To demonstrate the utility of our barcoded RVdG circuit mapping strategy in a biological circuit, we prepared
149 organotypic slice cultures from the human cerebral cortex during the second trimester of prenatal development,
150 spanning gestational weeks (GW) 16-22. At this developmental stage, puncta positive for the postsynaptic
151 marker PSD-95 are enriched in the marginal zone and along structures resembling dendrites in the cortical
152 plate, while puncta positive for the presynaptic markers synaptophysin (SYP) and VGLUT1 are concentrated in
153 the marginal zone and the upper layer of the subplate (Figures 3A, 3B, and S2A), consistent with previous
154 studies investigating the distribution of synapses at this age^{20,21}. To perform circuit mapping using barcoded
155 RVdG, slices were first infected with a lentivirus helper on day 0 (DIV0) which encodes an optimized RV
156 glycoprotein (oG), which is necessary for trans-synaptic spread, TVA, an avian receptor that enables selective
157 infection by EnvA-pseudotyped viral particles, and the fluorescent reporter GFP or mGreenLantern-KASH
158 (mGL-KASH) (Figure 3C; STAR Methods). On DIV3, slices were transduced with RVdG expressing either
159 dTomato or oScarlet-KASH (Figure 3C and S2B–S2H). By DIV8, we observed both double-labeled starter cells
160 and putative presynaptic non-starter cells positive for RVdG only (Figures 3D–3G and S2B–S2H).
161 Immunohistochemistry revealed that most of the infected cells expressed postmitotic neuronal markers NeuN
162 and NEUROD2, suggesting that the majority of RVdG+ starter and non-starter cells are glutamatergic neurons
163 (Figures 3D–3F and S2B–S2H).

164 **Helper virus– and RVdG–infected cells are predominantly layer 2/3 excitatory neurons**

166 To achieve a more granular classification of RVdG-infected cell types, we performed single-cell RNA
167 sequencing (scRNA-seq). Tissue slices from seven individuals were dissociated into single cells and FACS-
168 sorted based on the expression of RVdG-encoded dTomato or oScarlet-KASH (Figures 4A, S3A, and S3B). In
169 a subset of slices, we also collected dTomato/oScarlet-negative cells to serve as uninfected controls. We
170 captured a total of 17,343 RVdG-infected cells and 7,446 uninfected cells, after filtering based on quality
171 control metrics (STAR Methods). We used principal component analysis to reduce the dimensionality of the
172 data and Harmony²² for dataset integration. We visualized the transcriptomic data in high dimensional space
173 using uniform manifold approximation and projection²³ (UMAP) and used Louvain clustering²⁴ to group cells
174 into distinct clusters based on their gene expression profiles (Figure 4B). We annotated the resulting

175 transcriptomic clusters based on expression of canonical marker genes to identify the major cell types: layer
176 2/3 neurons (L2/3 ExNs) that express BHLHE22^{25,26} and CUX2^{27–30}, layer 4 neurons (L4 ExNs) that express
177 BHLHE22^{25,26} and RORB^{31,32}, layer 5/6 and subplate neurons positive for TLE4^{30,33–36} and CRYM^{30,37–39}
178 (L5/6/SP ExNs), DLX5/GAD1+ inhibitory neurons (InNs)^{40–42}, PDGFRA+ oligodendroglia (OL)^{43,44}, EOMES+
179 intermediate progenitor cells (IPCs)^{45–47}, HES1+ radial glia (RG)^{48–50}, astrocytes enriched for AQP4^{48,51–53} and
180 GFAP^{54–56} (AC), and MKI67+ dividing progenitors⁵⁷ (DIV) (Figures 4C-D, S4 and Table S3). Each cell type was
181 represented in each sample (Figure 4E). RVdG-infected cells were further divided into starter and non-starter
182 populations based on the expression of lentiviral helper transcripts (STAR Methods). Compared to uninfected
183 cells, RVdG-infected cells were enriched in GABAergic, L2/3, and L4 ExNs and depleted of RG and astrocytes
184 (one-sample t-test, $p=0.00088$, $4.304e-09$, $6.784e-05$, $1.5968e-07$, and $6.432e-06$) (Figures 4F and 4G).
185 Similarly, when compared to uninfected cells, helper-infected cells were enriched in L2/3 ExNs and depleted of
186 RG and progenitors (one-sample t-test, $p=0.00088$, 0.01650912 , $2.464e-05$, and $3.408e-07$) (Figure 4G).

188 **RVdG-infected neurons exhibit strain-dependent toxicity**

189 Prior work has suggested that the CVS-N2c strain of RVdG is less toxic and spreads more efficiently across
190 synapses compared to the more commonly used SAD-B19 strain⁵⁸. Since our dataset includes slices infected
191 with both the SAD-B19 strain ($n=5$ individuals at GW 16, 20, 20, 21, and 22) and the CVS-N2c strain ($n=2$
192 individuals at GW 19 and 21), we next set out to quantify strain-dependent toxicity profiles and cell type biases.
193 In total, we identified 5,840 cells from SAD B19 RVdG-infected slices and 11,503 cells from CVS-N2c RVdG-
194 infected slices after filtering based on quality control metrics (Figure 5A and STAR Methods).
195 We observed that samples infected with either CVS-N2c or SAD B19 RVdG showed an enrichment of neuronal
196 populations, particularly L2/3 ExNs, over glial cells compared to uninfected cells (Figure 5B). This enrichment
197 is likely due, in part, to the use of the human synapsin I promoter to drive helper virus transcripts, which biases
198 starter cell infection toward neurons⁵⁹, coupled with preferential spread of RVdG trans-synaptically between
199 neurons^{60,61}. Gene set enrichment analysis (GSEA) revealed an enrichment in inflammatory and immune
200 response pathways in the SAD B19 datasets (Figures 5C-5D, S5). These signatures were primarily driven by a

201 population of inflammatory astrocytes that were present only in the SAD B19 datasets ([Supplement 5J and 5L](#)),
202 in line with previous studies^{62–64}.

203 We also sought to assess strain-dependent toxicity using targeted whole-cell patch clamp recording of
204 cells with neuronal morphology. SAD B19-infected cells showed blebbing of the axodendritic processes and
205 were less likely to fire action potentials compared to CVS-N2c–infected cells ([Figures 5E, 5F and S6](#)). Intrinsic
206 biophysical properties including cell capacitance, input resistance, and resting membrane potential were more
207 variable in SAD B19–infected compared to CVS-N2c–infected neurons ([Figure 5G–5I](#)), and the resting
208 membrane potential was significantly depolarized in SAD B19–infected compared to CVS-N2c–infected
209 neurons ([Figure 5I](#)). Thus, while similar transcriptomic cell types are present in both the SAD B19–infected and
210 CVS-N2c–infected cell populations, SAD B19-infected cells exhibit both gene expression electrophysiological
211 signatures toxicity compared to CVS-N2c-infected cells.

212 213 **The MS2-MCP-KASH system can be used to target RVdG-encoded barcodes to the nuclear membrane** 214 **for snRNA-seq readout**

215 Prior versions of barcoded RVdG virus are compatible with scRNA-seq readout; however, adult brain tissue is
216 more commonly studied using snRNA-seq due to loss of susceptible cell types such as projection neurons
217 during single cell dissociation^{58,65}. RVdG viral replication and transcription occurs entirely in the cytoplasm,
218 preventing readout of RVdG-encoded barcodes from nuclei⁶⁶. To overcome this limitation, we leveraged MS2
219 tagging, which takes advantage of strong interactions between MS2 bacteriophage coat protein (MCP) and a
220 defined RNA sequence that forms a hairpin *in situ*^{67,68}. First, we cloned an MCP tagged with the fluorescent
221 protein oScarlet and the KASH outer nuclear membrane localization domain⁶⁹ into the fourth open reading
222 frame of the CVS N2c RVdG genome. We additionally cloned the 6x tandem MS2 hairpin sequence into the 3'
223 UTR of the MCP-oScarlet-KASH sequence proximal to the barcode sequence. Together, these two
224 modifications provide a mechanism to target both the fluorescent reporter oScarlet and the RVdG-encoded
225 barcode transcripts to the outer nuclear membrane, facilitating barcode recovery from sorted nuclei ([Figures](#)
226 [6A–6B](#)).

To determine how well we could capture RVdG barcodes in nuclei using MS2-KASH tagging, in a subset of cases we isolated nuclei for snRNA-seq and whole cells for scRNA-seq in parallel from adjacent slices infected with the CVS-N2c-MS2-KASH-oScarlet RVdG (Figures 6C and S3C). Our snRNA-seq dataset included all of the major transcriptomic cell types we identified using scRNA-seq, indicating that nuclei isolations preserve the cellular diversity observed in whole cell dissociations (Figures 6D-6E). Within these paired samples, we identified 1,141 nuclei and 9,332 cells after filtering based on quality control metrics (STAR Methods). We performed targeted amplification of the RVdG barcodes (STAR Methods) and quantified RVdG barcodes after deduplication based on cell/nucleus barcode and UMI. In total, we detected 451,324 unique cell:barcode combinations and 115,635 unique nucleus:barcode combinations. We detected slightly fewer UMIs per unique cell/nucleus:barcode combination in nuclei compared to cells (Figure 6F; median=1 UMIs per unique cell:barcode combination, median=1 UMIs per unique nucleus:barcode combination) but similar numbers of total barcode UMIs in both (Figure 6G; median=135 total barcode UMIs per cell, median=120 total barcode UMIs per nucleus). There was a positive correlation between total barcode UMIs detected and number of unique barcodes detected in both cells and nuclei (Figure 6H). Taken together, these findings demonstrate that RVdG barcode capture from nuclei is tractable and only moderately less sensitive than barcode capture from cells. The ability to use snRNA-seq readout of RVdG barcodes provides a path forward for RV-based circuit mapping in more mature tissues that are not amenable to whole cell dissociation, such as the adult human brain.

Reduction of ambient barcode sequences using UMI thresholding

Ambient RNA in a cell/nucleus suspension can be aberrantly counted along with a cell's native mRNA during droplet-based sc/snRNA-seq, leading to cross-contamination of transcripts between different cell populations⁷⁰. While low expression of ambient transcripts may be insufficient to alter the cell type classification of a sequenced cell or nucleus, it could potentially lead to false positive connections when reading out connectivity using RVdG-encoded barcodes. Therefore, we sought to establish quality control metrics for assigning RVdG barcodes to cells and nuclei while minimizing potential artifacts due to ambient RNA transcripts. In single cell datasets we detected RVdG barcodes in 5.85% of empty droplets, defined as containing ≤ 10 total UMIs in the

paired cell transcriptome library (Figure 7A). Empty droplets contained fewer total barcode UMIs (median=136 in real cells, median=1 in empty droplets; Figure 7B) and fewer unique barcodes compared to real cells (median=99 in real cells, median=1 in empty droplets; Figures 7C and 7D). To minimize the risk of inferring false positive connections due to ambient barcodes, we aimed to identify a UMI threshold to remove ambient barcodes from downstream analysis (Figure 7E). We found that implementing a threshold of ≥ 3 UMI counts per cell:barcode combination was sufficient to filter out more than 90% of empty droplets while retaining more than 90% of cells (Figure 7E). We performed a similar analysis on our datasets generated from single nuclei dissociations which revealed RVdG barcodes in 5.06% of empty droplets (Figure 7F). Real nuclei also had more total barcode UMIs (median=116 in real nuclei, median=1 for empty droplets) and more unique barcodes (median=100 in real nuclei, median=1 in empty droplets) compared to empty droplets (Figure 7G, 7H, and 7I). Applying the threshold to keep only nucleus:barcode combinations with a UMI count ≥ 3 filtered out approximately 98% of empty droplets while retaining 87% of nuclei for downstream analysis (Figure 7J). Based on these results, only cell/nucleus:barcode combinations with ≥ 3 UMIs were used for downstream connectivity analysis.

Barcoded RVdG circuit mapping reveals the emergence of cell type–specific connectivity motifs in second trimester human cerebral cortex

To assess the emerging connectivity matrix in second trimester human cerebral cortex, we pooled together our single-cell and single-nuclei sequencing datasets and their corresponding RVdG barcodes (Table S4). We identified a total of 12,036 unique RVdG barcodes (Figure S7A). To identify putative connections we identified networks of cells that shared a common barcode ('barcode networks'), and annotated cells as starter or non-starter cells based on expression of helper virus (STAR Methods). Barcode networks with no starter cell were excluded from further analysis. We identified 5,047 barcodes in 1,230 starter cells: 2,762 barcodes were found in a single starter cell and 2,285 barcodes were found in multiple starter cells (Figure 8B). The barcode

278 networks containing multiple starter cells were excluded from further analysis due to the ambiguity of
279 connection directionality and possibility of polysynaptic spread through multiple starter cells. Of the 2,762
280 barcodes found in a single starter cell, 1,102 were also found in at least one non-starter cell. We proceeded to
281 infer connectivity using only the 457 barcode networks containing a single starter cell and at least one non-
282 starter cell ('single starter networks'), where directionality can be determined based on retrograde spread of
283 RVdG virus¹. To prevent calling duplicate connections when multiple barcodes are shared between two cells,
284 we collapsed all instances of connections between the same two cells into a single count. Distinct barcode
285 networks with converging cells were then collapsed into singular networks, and duplicate connections were
286 merged into one labeled connection (Figure 8A). After collapsing all duplicate connections, we identified 457
287 singular networks consisting of 4,331 directed connections centered around individual starter cells (median=5
288 cells per network, Figure 8C). The cell type composition in each network was similar across different network
289 sizes (Figure 8D-E) and the vast majority of connections (3622/4331, 83.6%) were between neuronal cell
290 types.

291 Next we merged singular networks together to visualize them as graphs in which each cell appears only
292 once, by linking non-starter cells that could exist in multiple singular networks (Figures 8F and S8). A plurality
293 of connections were between L2/3 ExNs (n=2039/4331, 47.08%) and L2/3 neurons received the largest
294 proportion of inputs compared to other cell types (n=3087/4331, 71.28%; Figure 8G, S7B). Given that L2/3
295 ExNs are also the most prevalent cell type in our dataset, irrespective of RVdG infection (Figures 4G and 5B),
296 we next asked how the observed connectivity matrix compared to a null connectivity matrix with random
297 connections between the defined starter cell population and the pool of possible interacting cells. Specifically,
298 the connectivity expected by chance between any two cell types was modeled as a binomial distribution
299 considering the proportions of those cell types in the starter and uninfected populations (STAR Methods). After
300 controlling for cell type proportions, neuronal cell types were still enriched in connections and glial cell types
301 were depleted of connections (Figure 8H), consistent with RVdG spread being largely restricted to chemical
302 synapses in the developing human brain. The strongest enrichment was observed among GABAergic neurons,
303 which also target all other neuronal cell types more often than predicted by chance. In contrast, L5/6/SP
304 receive inputs from all neuronal populations, but preferentially target other L5/6/SP neurons. Taken together,

305 these findings suggest that cell type–specific circuit motifs are already beginning to emerge in midtrimester
306 human brain development.

308 **DISCUSSION**

309 Understanding neuronal connectivity at the level of molecularly defined cell types remains a key challenge in
310 neuroscience. Sequencing-based approaches to connectivity mapping provide a potential path forward for
311 scalable circuit mapping by leveraging the power and throughput of single cell genomics. In particular,
312 barcoded RVdG has recently emerged as one strategy for integrated circuit mapping and molecular
313 interrogation of the mapped cells³⁻⁵, but its application has been limited by the degree of barcode complexity
314 and an inability to reliably detect RVdG transcripts in dissociated single nuclei⁷¹. Here we introduce an RVdG
315 packaging protocol that is specifically tailored to improve barcode complexity, increasing the number of cells
316 that can be mapped simultaneously in one experiment by several orders of magnitude compared to prior
317 protocols. We also describe a strategy for nuclear localization of RVdG barcodes that enables snRNA-seq
318 readout of the RVdG-encoded barcodes. Lastly, we demonstrate the power of these new tools by mapping
319 local cell type–specific connectivity in organotypic slice cultures of the developing human cerebral cortex. By
320 converting the problem of synaptic connectivity into a problem of barcode sequencing, barcoded RVdG circuit
321 mapping has the potential to transform connectomics into a routine experiment that can be performed in any
322 lab with modest resources, making it possible to explore how circuits differ between treatment conditions, in
323 disease states, between the sexes, across the lifespan and across species.

324 Barcode complexity is a limiting feature of all barcoded viral tracing strategies⁷², but has been
325 especially problematic for barcoded RVdG circuit mapping due to the low efficiency of viral barcode recovery
326 during the packaging process³. We identified two key factors that improve the complexity of barcoded RVdG
327 libraries: transfection reagent and packaging cell line. Specifically, of the options we tested, Lipo3000 and PEI
328 MAX offer a substantial improvement in the percentage of cells recovering active RVdG particles compared to
329 other reagents including Lipo2000^{3,5} or Xfect⁴. A direct comparison of library complexity between RVdG
330 packaged in Lipo3000 and Lipo2000 revealed a significant improvement in barcode complexity in libraries that
331 were packaged in Lipo3000, suggesting that improved transfection efficiency directly translates to improved

barcode complexity. We also found that HEK293T⁴ is more efficient at rescuing RVdG compared to the BHK21-derived B7GG fibroblast line³ and Neuro2A⁵, in line with previous work^{6,73}. One potential argument for packaging RVdG in Neuro2A cells is that it may enhance neurotropism and decrease neurotoxicity⁵⁸. However, at least one recent study found no significant difference in connectivity data acquired using RVdG recovered in HEK293T cells or Neuro2A cells¹⁷. In addition, we show that a HEK293T cell line that stably expresses oG (HEK-GT¹⁷) further improves uniformity of barcode libraries. There could be several reasons for this. First, the dynamic range of rabies G expression is likely narrower in the cell line compared to plasmid-based transient transfection⁷⁴. Because rabies G confers expression-level dependent spread^{18,75}, this may provide a more fair competition between expanding barcode clones. Additionally, oG shows up to 20-fold greater efficiency in promoting transsynaptic spread¹⁸ compared to SAD B19 G, which is traditionally used for packaging RVdG. Finally, transfecting fewer plasmids may improve overall transfection efficiency⁷⁶. New transfection reagents, additives, and cell lines that stably expresses the additional genes required for RVdG packaging may further enhance barcoded RVdG library complexity.

We used a defined barcode whitelist¹¹ in lieu of randomer^{3,5} or semi-randomer⁴ barcodes which can require complex probabilistic models to determine whether similar but non-identical barcodes represented the same or distinct sequences. Using a pre-defined whitelist of unique sequences allows us to ensure that any two barcodes differ by at least 6 bp (Hamming distance ≥ 6), making barcode identification robust to sequencing errors or mutations that arise during virus production. Furthermore, by using the whitelist as a reference genome, barcodes can be aligned using standard transcriptomic aligners (e.g., STAR, bowtie2), streamlining the process and reducing the computational complexity typically required to collapse similar barcode sequences⁴. However, our barcodes are 61 bp in length, requiring longer sequencing reads that may preclude spatial transcriptomic readout used by several groups for barcoded RVdG circuit mapping^{5,77}. New barcode strategies that can balance a high Hamming distance with short overall barcode length might further streamline the barcode design to such that it can be read out using any platform.

Rabies virus is an RNA virus that is localized primarily within the cytoplasm^{9,10} and prior studies utilized whole-cell single-cell transcriptomics for barcode recovery. However, more mature brain tissue and flash frozen tissue cannot be easily dissociated into intact cells. We developed a method for localizing barcoded

359 transcripts to the nucleus by leveraging MS2 tagging^{67,68} guided by the KASH nuclear localization signal, and
360 demonstrated efficient recovery of RVdG-encoded barcode transcripts from single nuclei. It is possible that
361 tethering the barcode transcripts to a different nuclear protein, such as histone 2B (H2B), could further improve
362 barcode recovery in nuclei.

363 We focused on two commonly used RVdG strains: SAD B19 and CVS-N2c. Consistent with prior
364 reports, our data suggest that the CVS-N2c strain is less toxic than the SAD B19 strain⁵⁸. Despite this impact
365 on cell health, we were able to generate high-complexity libraries using both strains. Circuit mapping
366 experiments showed that both strains captured similar proportions of cell types. Further experiments aimed at
367 elucidating nuanced differences in the tropism of different RVdG strains, and the rabies G that drives trans-
368 synaptic spread, will be important to be able to compare RVdG-inferred connectomes to each other and to
369 ground truth wiring diagram of a circuit, which may be difficult to know a priori.

370 We applied barcoded RVdG to explore connectivity in organotypic slice cultures of the human brain
371 during the second trimester of gestation, a developmental window during which neuronal connectivity is
372 actively being established. We observed an enrichment in connectivity between neuronal cell types compared
373 to non-neuronal cell types, supporting the idea that rabies virus is biased towards trans-synaptic spread. We
374 observed the greatest enrichment in connectivity between GABAergic neurons, and from GABAergic to other
375 neuronal populations. Previous studies have demonstrated the critical role of depolarizing GABAergic signaling
376 in the formation of AMPA receptor-mediated glutamatergic circuitry⁷⁸⁻⁸¹. This mechanism is thought to be
377 mediated by synaptic release of GABA onto maturing glutamatergic neuronal populations, and our data
378 suggest that this may be one of the most prominent circuit motifs during mid-gestation in humans. We also
379 observed enrichment in connectivity from all neuronal populations onto L5/6/SP ExNs, consistent with previous
380 work^{78,82-84}. In particular, the enrichment in connections from L4 to L5/6/SP may correspond to transient
381 synapses formed during the establishment of the thalamus-subplate-thalamus circuit. We also identify shared
382 barcodes between neurons and non-neuronal cell types, suggesting RVdG spread is not entirely restricted to
383 mature synapses^{3,60,61,85}. Shared barcodes between cells may also arise following division of a single infected
384 cell, such as an IPC, RG, or oligodendrocyte precursor cell (OPC, a subset of OL in our dataset). Disentangling
385 the contribution of cell division and trans-synaptic spread in actively dividing cell populations may be possible

386 in future studies by using two barcode systems in parallel - one for tracking cell lineage (e.g. a barcoded
387 lentivirus) and another for tracking connectivity (barcoded RVdG).

388 In summary, we report an optimized protocol for generation of high-complexity barcoded RVdG that is
389 compatible with both single-cell and single-nucleus RNA-sequencing readout. This powerful new tool enables
390 probing synaptic connectivity at unprecedented scale and molecular detail. Future applications of this tool may
391 help to reveal the organizational principles of brain circuits across species, ages, and disease states.

392 393 **ACKNOWLEDGEMENTS**

394 We thank members of the Nowakowski and Cadwell labs for providing helpful feedback throughout this project
395 and Ken Probst and Melissa Logies for assistance with figure layout and schematics. This work was supported,
396 in part, as grants from NIH: U01MH130700, R01NS123263, R01MH128364 and RF1MH125516 (to T.J.N.),
397 K08NS126573 and U01NS132353 (to C.R.C), Awards from the Klingenstein-Simons Fund in Neuroscience,
398 Broad Foundation and Sontag Foundation (to T.J.N.), the Shurl and Kay Curci Foundation (to T.J.N. and
399 C.R.C.), and the Weill Neurohub (to C.R.C.), and gifts from Schmidt Futures and the William K. Bowes Jr
400 Foundation (to T.J.N). This work was also supported by the National Science Foundation under award number
401 NSF #2134955 (T.N). T.J.N. is a New York Stem Cell Foundation Robertson Neuroscience Investigator. D.S.
402 was supported by the NSF Graduate Research Fellowship Program (GRFP). M.E.U was supported by the NSF
403 GRFP and the Hertz Foundation Fellowship. Sequencing was performed at the UCSF CAT, supported by
404 UCSF PBBR, RRP IMIA, and NIH 1S10OD028511 grants.

405 406 **AUTHOR CONTRIBUTIONS**

407 D.S., D.B., T.J.N., and C.R.C. conceptualized the study. D.S., H.H.L., M.E.U., K.L., D.L.B., and E.S.-B.
408 performed experiments. M.E.U., A.J.M., D.S., S.R. and C.R.C. performed analyses. D.S., M.E.U., A.J.M. and
409 C.R.C wrote and edited the manuscript with input from all other authors. C.R.C and T.J.N. supervised the study
410 and acquired funding to support this work.

411 412 **DECLARATION OF INTERESTS**

413 University of California San Francisco has filed a provisional patent application relevant to the technologies
414 described in this manuscript.

415

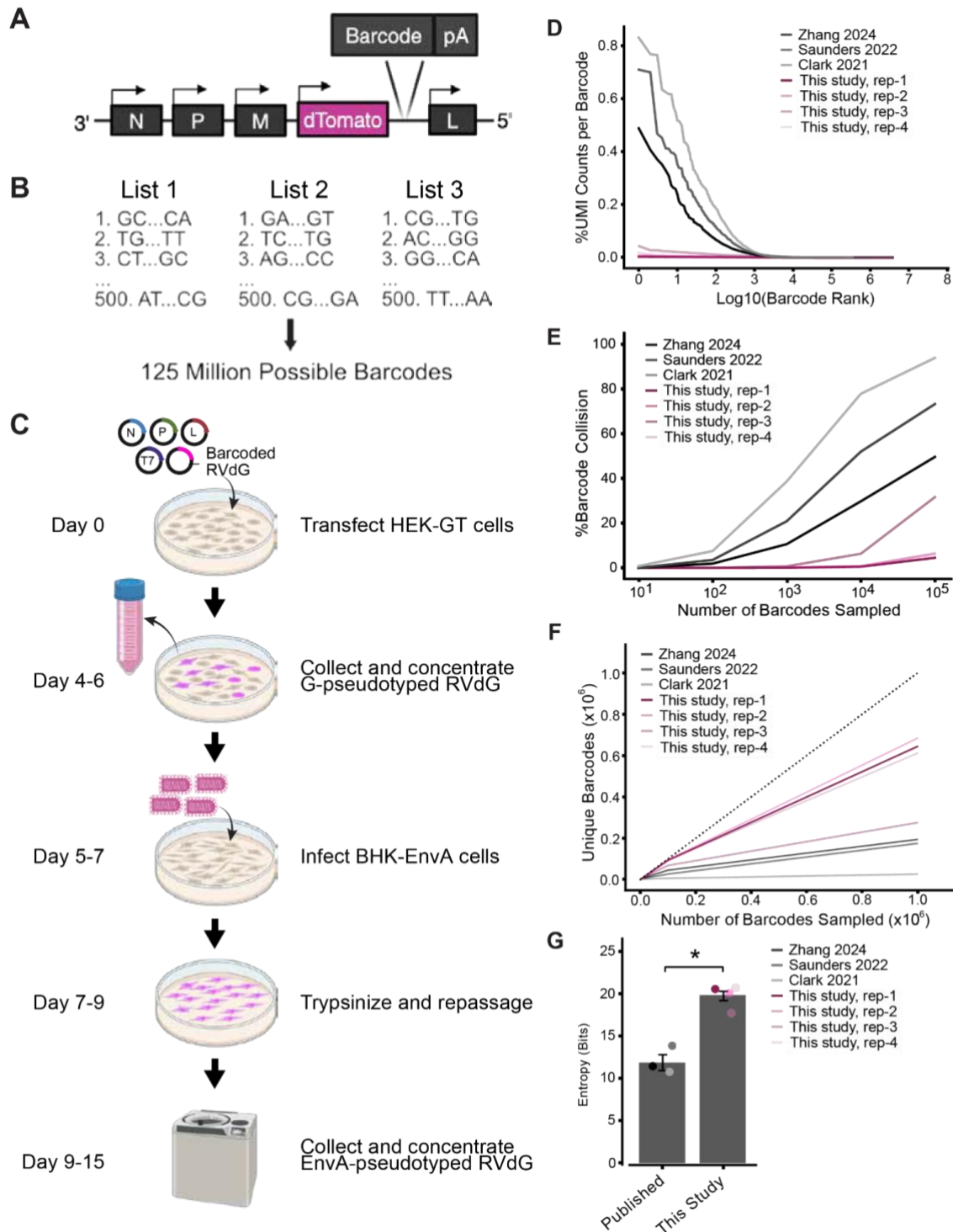
416 **DECLARATION OF GENERATIVE AI AND AI-ASSISTED TECHNOLOGIES**

417 During the preparation of this work, the authors used ChatGPT to suggest changes to improve the clarity of the
418 text. After using this tool or service, the authors reviewed and edited the content as needed and take full
419 responsibility for the content of the publication.

420

421 **FIGURES AND FIGURE LEGENDS**

422



423

424 **Figure 1. Generation of high-complexity barcoded RVdG libraries. A.** Location of barcode cloning site in

425 the rabies genome. **B.** Design of whitelist combinatorial barcode system. **C.** Schematic of barcoded RV

426 production protocol. **D.** Distribution of UMI counts per barcode normalized as a percent of total barcode UMI

427 counts. Barcoded RVdG libraries from this study are compared to previously published libraries³⁻⁵. **E.**
428 Percentage of simulated barcode collision events, or two cells receiving the same barcode by chance, as
429 a function of the number of infections simulated. Error bars are 95% confidence intervals for 50 iterations. **F.**
430 Number of unique barcodes identified as a function of sequencing depth. Error bars are standard deviation for
431 50 iterations. **G.** Shannon entropy (in bits) of each viral library. P-value computed using the Student's t-test
432 (* $p < 0.05$; published: $n = 3$ independent libraries, this study: $n = 4$ independent libraries [replicates 1 and 2 =
433 SAD B19, replicates 3 and 4 = CVS-N2c]).

434

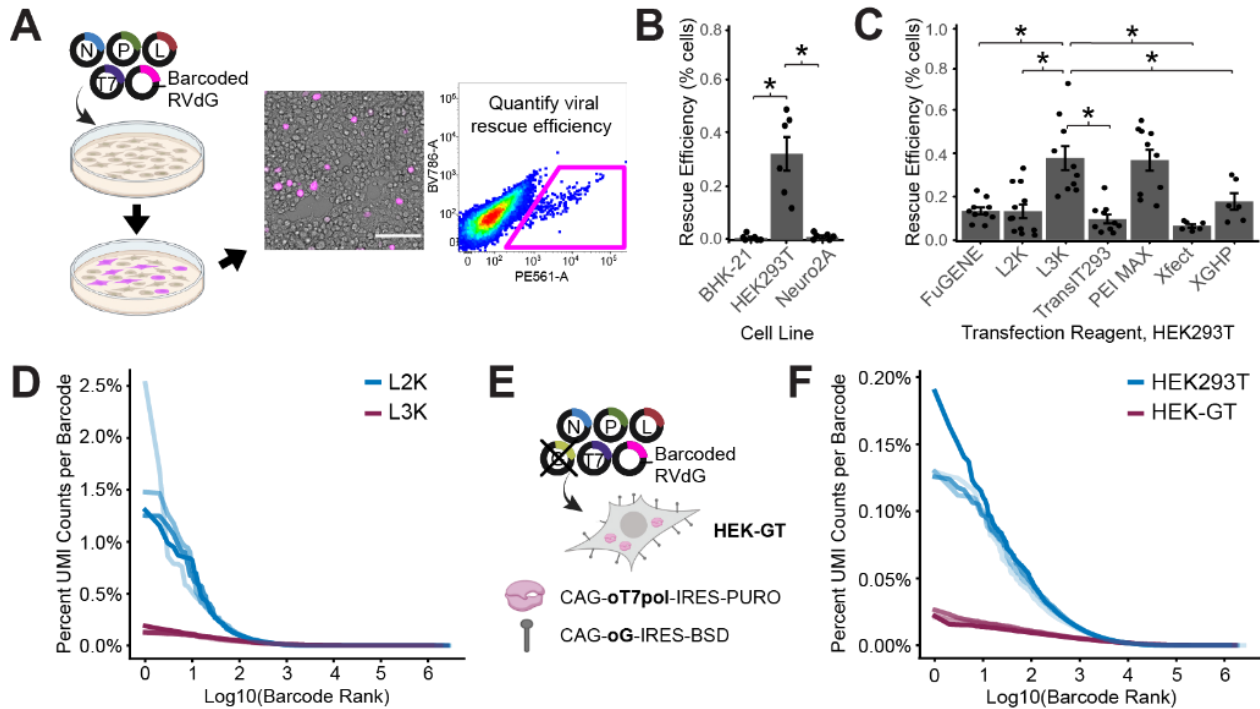


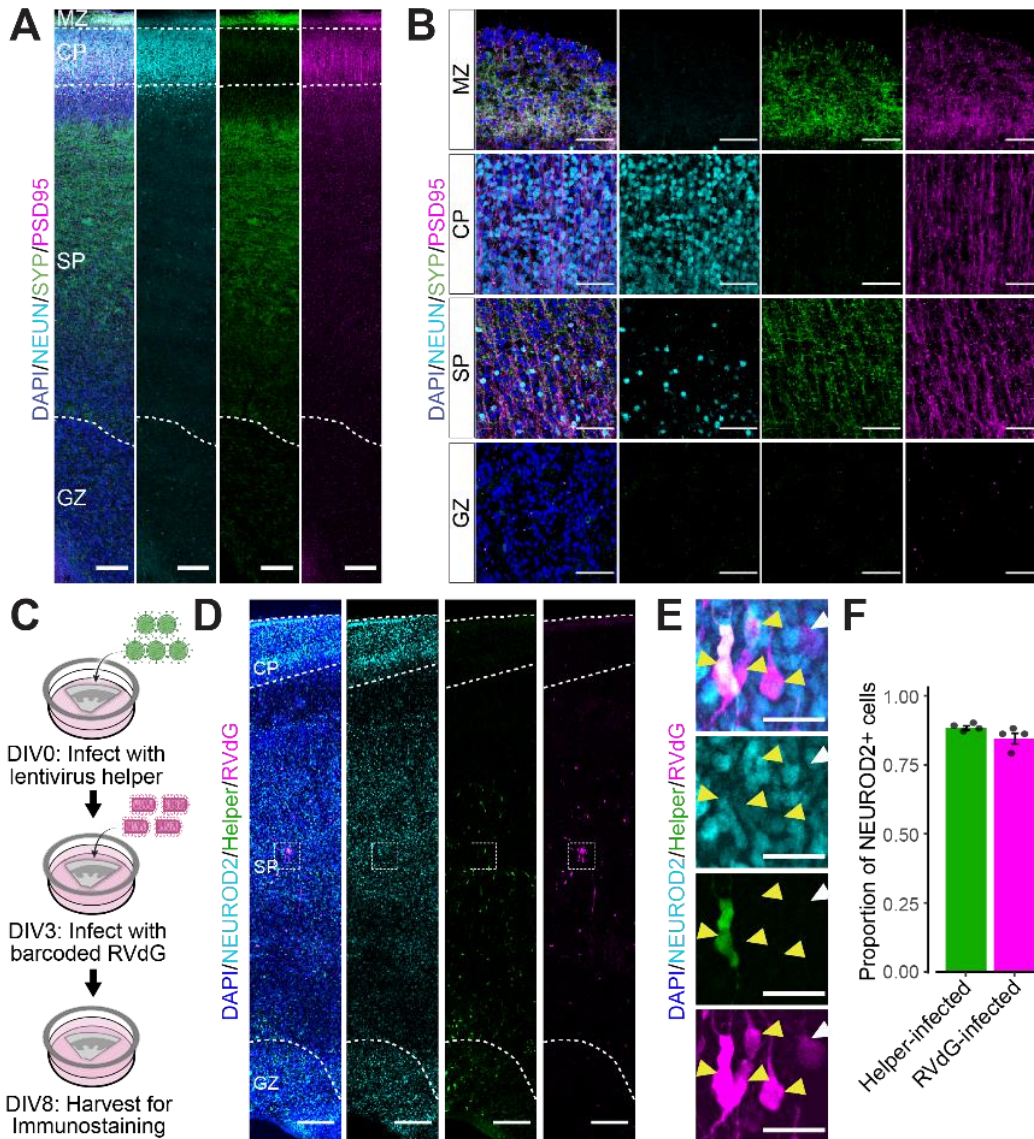
Figure 2. Viral packaging cell lines and transfection reagents are critical to generate high-complexity

barcoded RVdG. **A.** To assess packaging efficiency, cells are transfected with RVdG packaging plasmids in the absence of rabies G, and the percentage of cells producing rabies virus three days after transfection is measured by flow cytometry. **B.** Percentage of cells successfully producing RVdG three days after transfection using Lipofectamine 3000 (Lipo3000), comparing three commonly used packaging cell lines: BHK-21 (n=6 technical replicates), HEK293T (n=6 technical replicates), and Neuro2A (n=6 technical replicates). **C.** Percentage of HEK293T cells successfully packaging RVdG three days after transfection, comparing various commonly used transfection reagents: FuGENE HD (n = 10 technical replicates), Lipofectamine 2000 (n = 12 technical replicates), Lipofectamine 3000 (n = 10 technical replicates), TransIT-293 (n = 10 technical replicates), PEI (n = 10 technical replicates), Xfect (n = 6 technical replicates), and XtremeGene HP (n = 6 technical replicates). **D.** Distribution of UMI counts per barcode normalized as a percent of total UMI counts, comparing libraries generated from HEK293T cells using Lipo3000 (n=4 technical replicates) and Lipofectamine 2000 (Lipo2000, n=4 technical replicates). Transfection for virus packaging included rabies G. **E.** Schematic of virus packaging using HEK-GT cell line, which was engineered to stably express human

451 codon-optimized T7 polymerase (oT7pol) and the optimized rabies glycoprotein (oG), requiring fewer plasmids
452 to be co-transfected during packaging. **F.** Distribution of UMI counts per barcode normalized as a percent of
453 total UMI counts, comparing libraries generated in HEK293T cells (n=4 technical replicates) compared to HEK-
454 GT cells (n=4 technical replicates) using Lipofectamine 3000. In **(B)** and **(C)**, p-values are computed using
455 Wilcoxon Rank Sum with Bonferroni-Holm correction for multiple comparisons, *p<0.05.

456

457



458

459 **Figure 3. Helper virus– and RVdG–infected cells are predominantly neuronal in human prenatal**
 460 **organotypic slice cultures. A-B.** Full thickness tile scan **(A)** and high magnification images **(B)** of gestational
 461 week (GW) 22 cortex stained for pan-neuronal marker NeuN, presynaptic marker synaptophysin (SYP), and
 462 postsynaptic marker PSD95. **C.** Schematic of RVdG circuit mapping experiment in human prenatal organotypic
 463 slice cultures. **D-E.** Full thickness tile scan **(D)** and high magnification image **(E)** of slice stained for GFP (cells
 464 infected with helper virus), RFP (cells infected with RVdG), and NeuroD2. **F.** Quantification of the proportion of
 465 helper virus– and RVdG–infected cells that co-express NEUROD2 (n=4 slices from 4 different donors). Scale
 466 bars: 250 μ m in panels **(A,D)**, 50 μ m in panel **(B)**, 25 μ m in panel **(E)**.

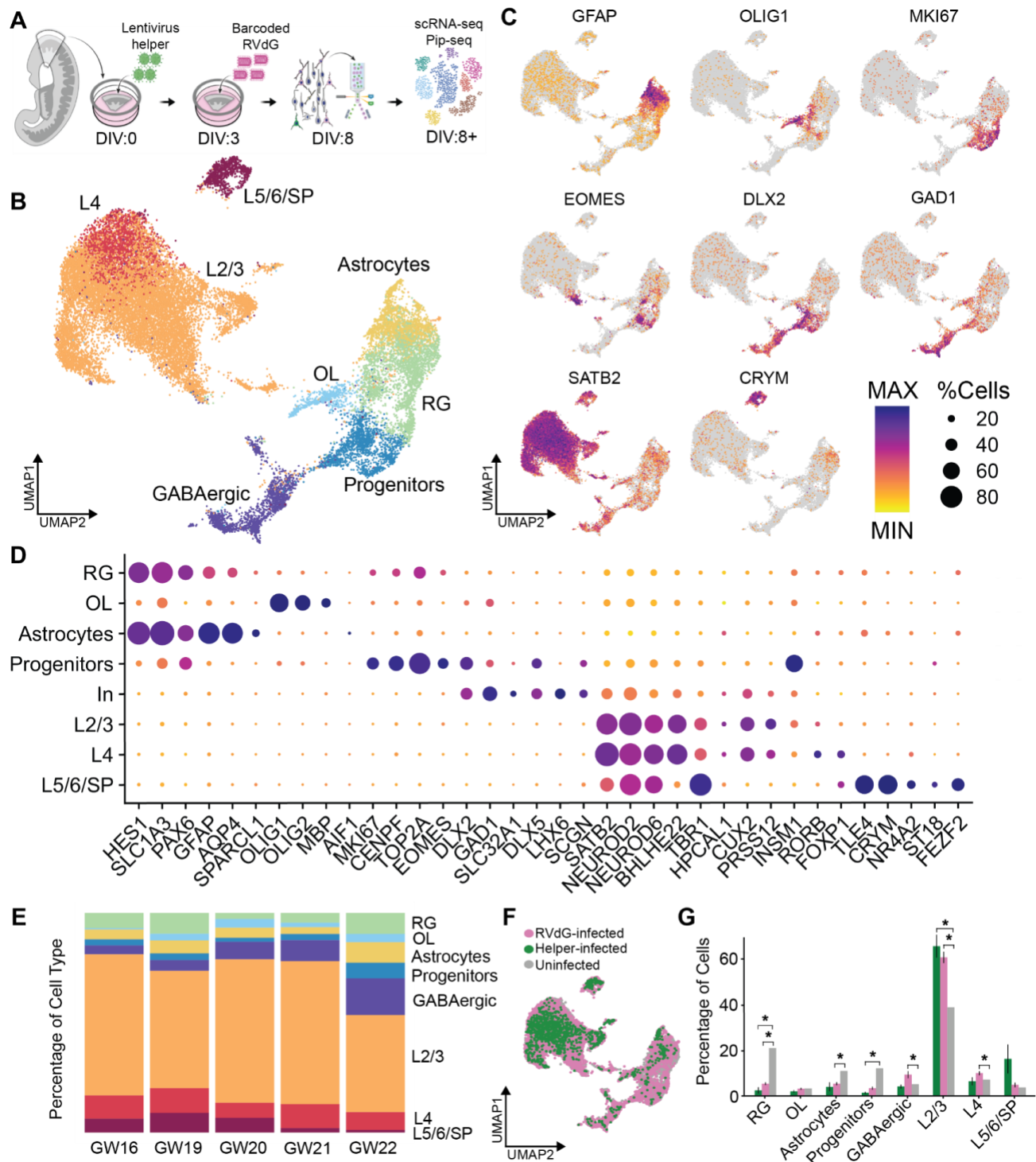


Figure 4. Helper virus- and RVdG-infected cells are predominantly layer 2/3 excitatory neurons. A.

Schematic of dissociated RNA-sequencing analysis of RVdG-infected tissue. **B.** UMAP of all pooled datasets

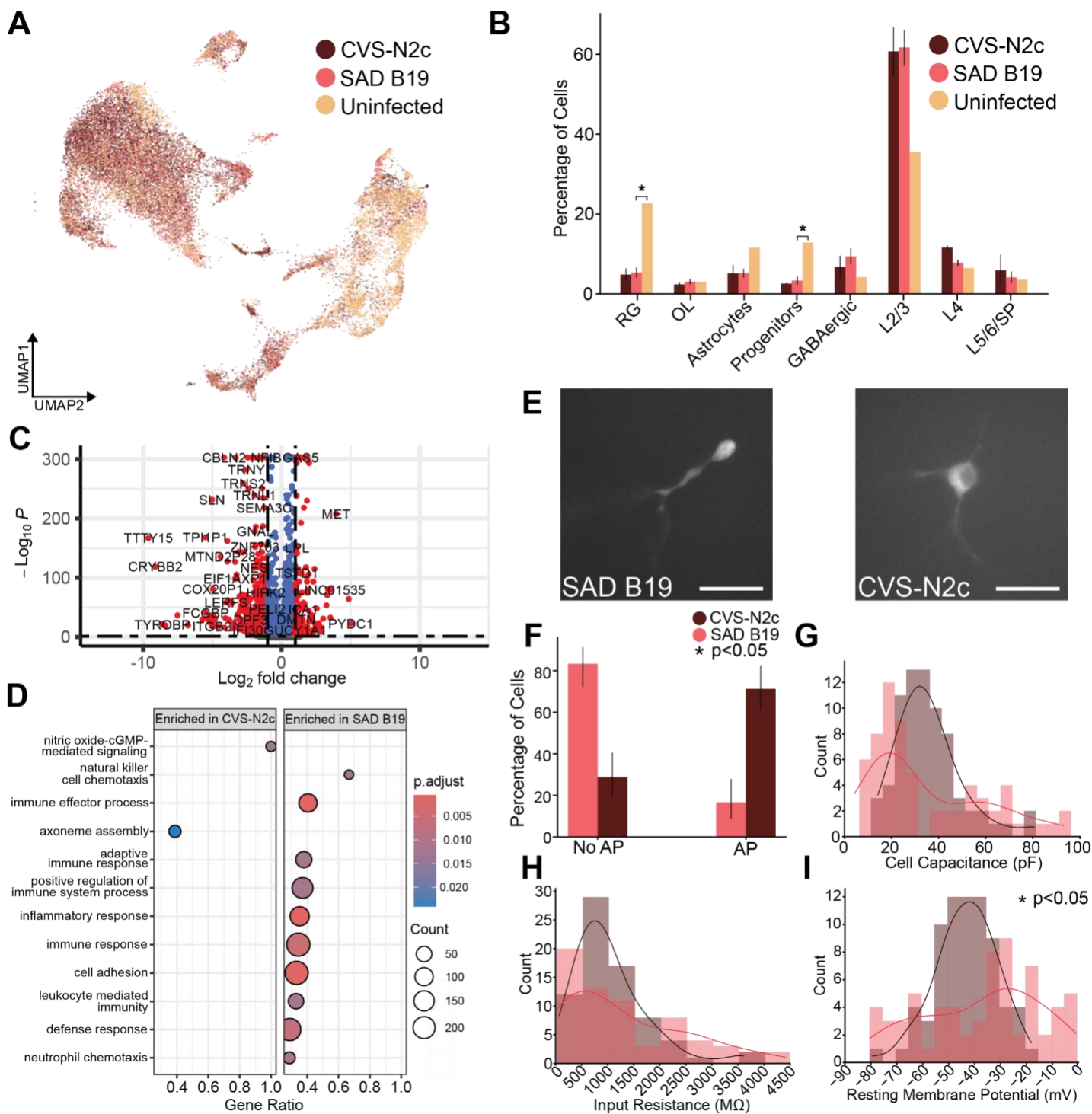
annotated with cell types. **C.** Feature plots showing expression of key cell type marker genes across clusters.

D. Dot plot of key marker genes across cell type clusters. Color indicates relative expression and size indicates

percent of expressing cells within the cluster. **E.** Stacked bar plot showing cell type distribution across sample

473 ages. **F.** UMAP with cells colored to match either RVdG and helper virus infection status. **G.** Proportions of cell
474 types among RVdG-infected, helper-infected or uninfected populations (bar plot indicates mean \pm SEM; p-
475 values computed using one sample t-test comparing RVdG-infected vs. uninfected and helper-infected vs.
476 uninfected and Bonferroni correction for multiple comparisons, *p<0.05; n=9 datasets for RVdG- and helper-
477 infected populations, n=1 dataset for uninfected population).

478



479

480

481

482

483

484

Figure 5. RVdG-infected neurons exhibit strain-dependent toxicity. A. UMAP visualization of transcriptomic cell types from SAD B19–infected, CVS-N2c–infected, and uninfected cell populations. **B.** Percentage of each major cell type among SAD B19–infected, CVS-N2c–infected and uninfected cell populations (bar plot indicates mean \pm SEM; * $p < 0.05$, one sample t-tests comparing CVS-N2c versus uninfected and SAD B19 versus uninfected within each cell type, with Bonferroni correction for multiple comparisons; $n = 2$

485 samples for CVS-N2c, n=5 samples for SAD B19, and n=1 sample for uninfected datasets). **C.** Volcano plot
486 showing differentially expressed genes between CVS-N2c– and SAD B19–infected cells. Positive \log_2 (fold
487 change) values indicate enrichment in CVS-N2c–infected cells, while negative \log_2 (fold change) values
488 indicate enrichment in SAD B19–infected cells. Genes with an adjusted p-value ≤ 0.05 are shown in red.
489 Genes from the GO term “Immune Response” are annotated. **D.** Gene set enrichment analysis reveals an
490 enrichment of immune response pathways in SAD B19–infected compared to CVS-N2c–infected cells. **E.**
491 Representative fluorescent images of SAD B19– and CVS-N2c–infected neurons. Scale bars, 30 μm . **F.**
492 Percentage of infected neurons capable of firing action potentials in response to direct current injection. Error
493 bars are 95% Clopper-Pearson confidence intervals. P-value computed using Fisher’s exact test (n=66
494 recordings for SAD B19, n=71 recordings for CVS-N2c). **G-I.** Intrinsic properties of recorded neurons including
495 cell capacitance (**G**), input resistance (**H**), and resting membrane potential (**I**). P-values computed using
496 Wilcoxon rank-sum test (* $p < 0.05$, n=66 recordings for SAD B19, n=71 recordings for CVS-N2c).

497

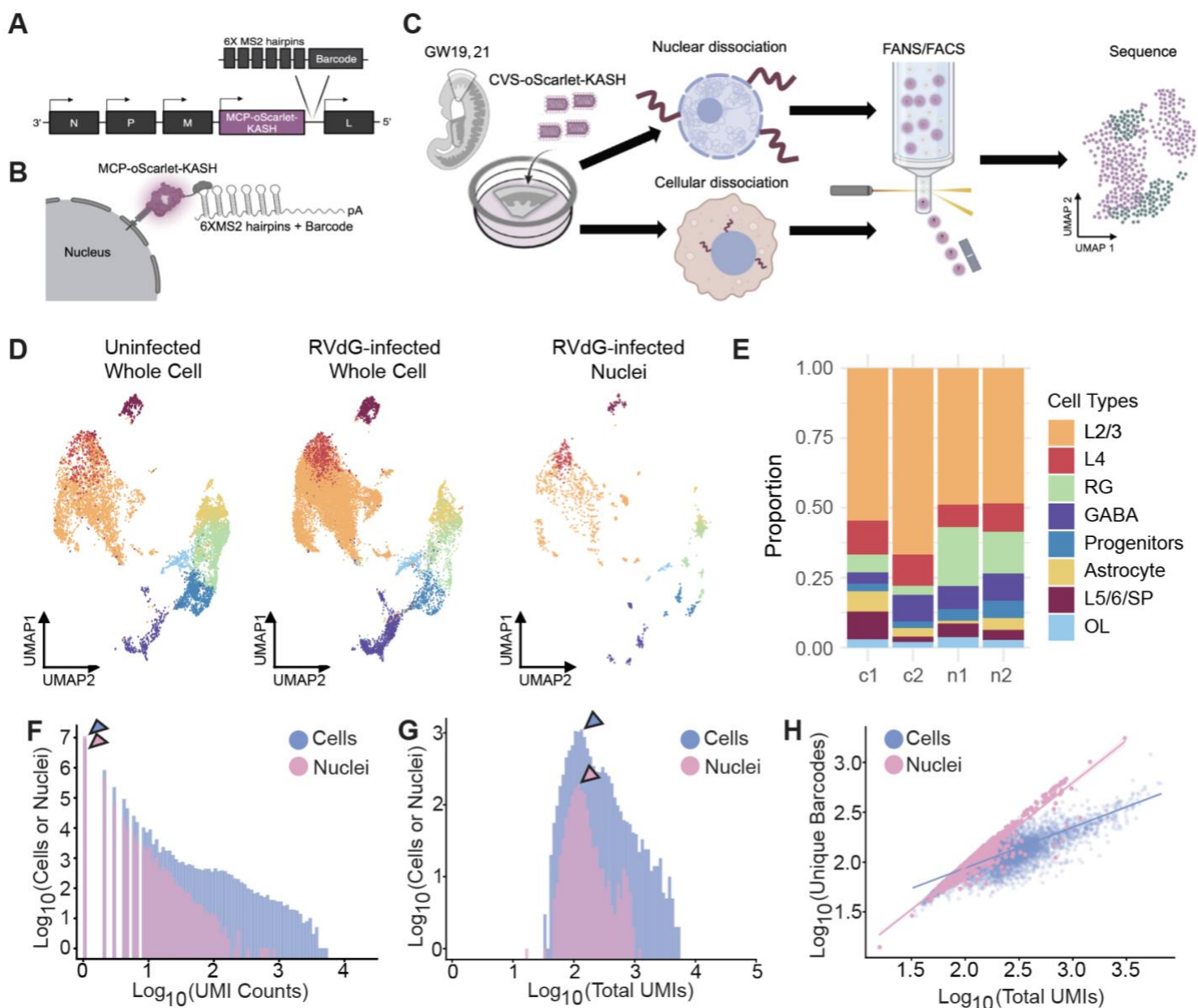
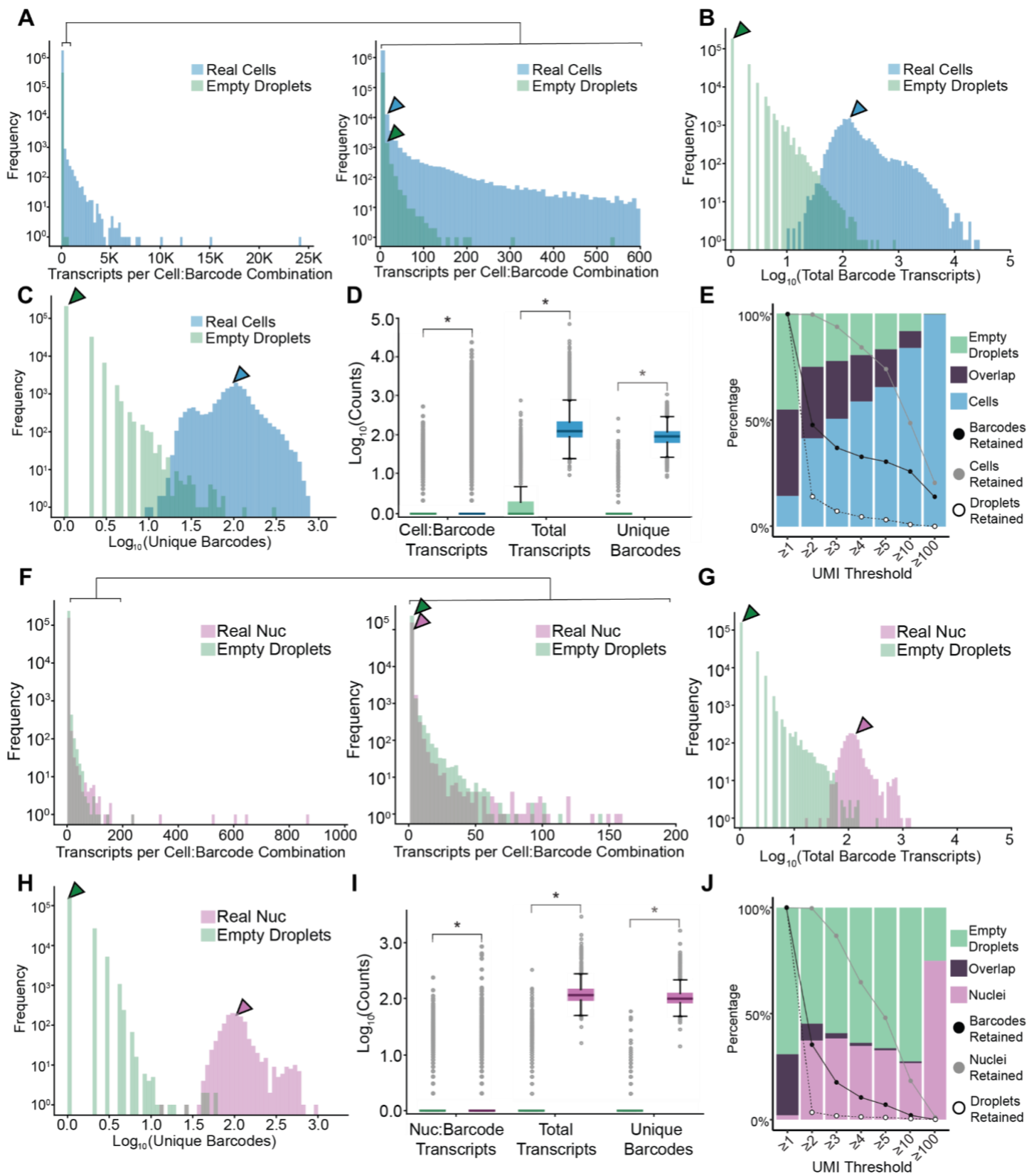


Figure 6. The MS2-MCP-KASH system can be used to target RVdG-encoded barcodes to the nuclear membrane for snRNA-seq readout. A. Location of barcode and nuclear localization signal cloning site in the rabies genome. **B.** Strategy for targeting of RVdG barcode transcripts to the nucleus utilizing KASH. **C.** Experimental paradigm in which slices from the same donors were dissociated into either single cells or single nuclei before enriching for RVdG-infected cells/nuclei for RNA-sequencing. **D.** UMAP visualizations of transcriptomic cell types from uninfected whole cell, RVdG-infected whole cell, and RVdG-infected nuclei datasets. **E.** Relative proportions of cell types captured by whole cell (c) and nuclear (n) datasets. **F.** Distribution of UMI counts for each unique barcode found within cells or nuclei. Medians are annotated by arrowheads (median=1 for cells, median=1 for nuclei). P-value computed using the Wilcoxon rank-sum test

508 (* $p < 0.05$). **G.** Distribution of total RVdG barcode UMIs captured per cell or nucleus. Medians are annotated by
509 arrowheads (median=135 for cells and median=120 for nuclei). P-value computed using the Wilcoxon rank-
510 sum test (* $p < 0.05$). **H.** Correlation between total number of UMIs detected and number of unique barcodes
511 detected per cell or nucleus with line of best fit. P-value computed using Spearman's Correlation (cell $R^2=0.66$,
512 nuclei $R^2=0.90$; * $p < 0.05$).

513

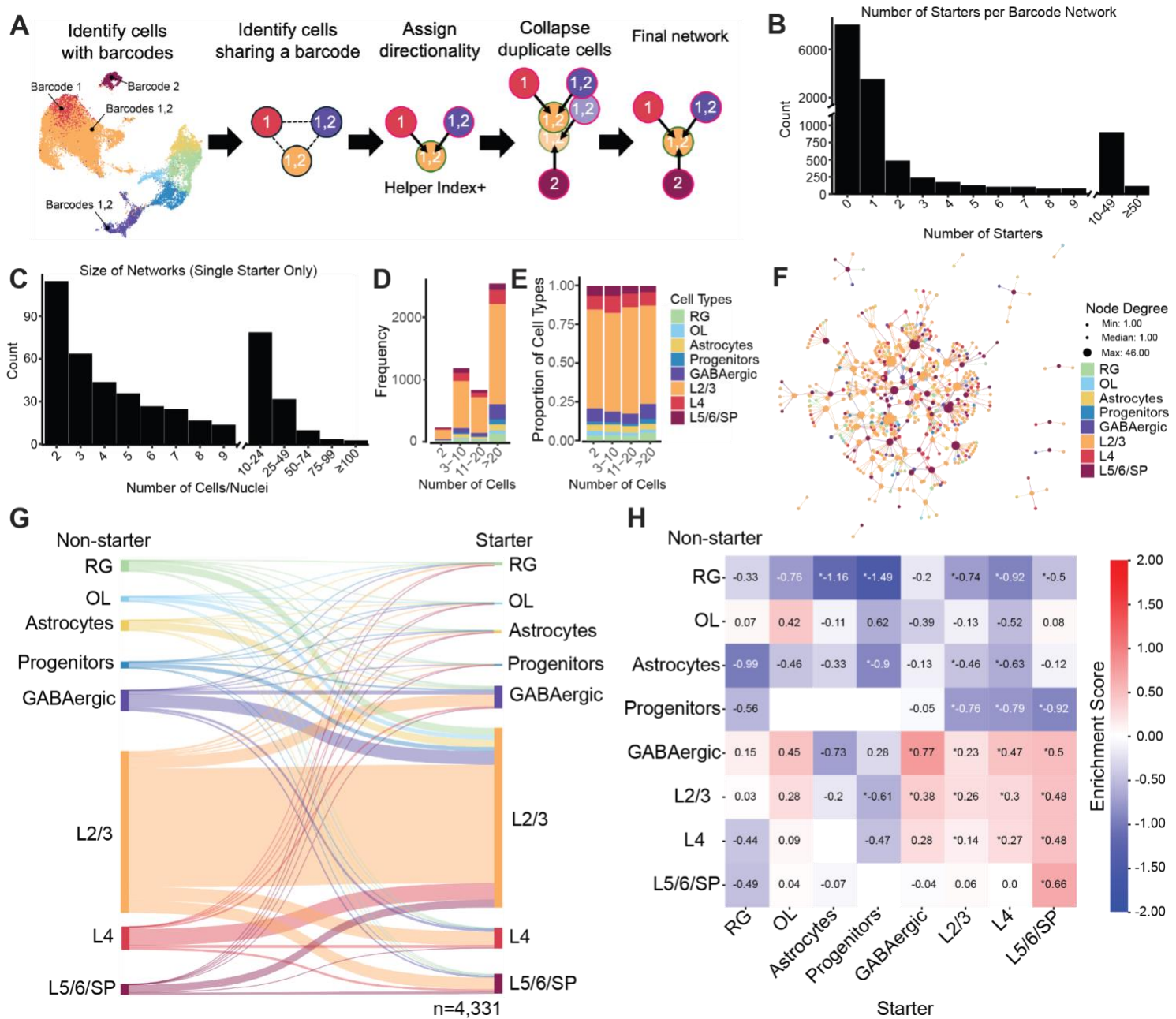


514

515

516 **Figure 7. Reduction of ambient barcode sequences using UMI thresholding. A.** Number of UMI
517 transcripts detected for every barcode in each cell or empty droplet from single cell dissociation experiments,
518 with magnified panel showing distribution from 0-600 UMIs on right (median=1 in both real cells and empty
519 droplets, indicated by arrowheads; n=1,740,015 cell:barcode combinations, n=315,450 empty droplet:barcode
520 combinations). **B.** Distribution of total barcode UMI transcripts detected per cell or empty droplet (median=136
521 in real cells, median=1 in empty droplets, indicated by arrowheads; n=16,036 cells, n=253,000 empty droplets).
522 **C.** Number of unique barcodes detected per cell or empty droplet (median=99 in real cells, median=1 in empty
523 droplets, indicated by arrowheads; n=16,036 cells, n=253,000 empty droplets). **D.** Number of UMI transcripts
524 per each barcode, total barcode UMI transcripts, and number of unique barcodes per cell or empty droplet. Box
525 plot shows median and interquartile range (IQR) of data in **(A–C)**. **E.** Stacked bar plot showing fraction of
526 barcodes uniquely found in empty droplets, cells, or both groups after implementing the indicated UMI
527 threshold. Percent of RVdG barcodes, cells, and empty droplets retained after implementing the UMI threshold
528 is overlaid. **F.** Number of UMI transcripts detected for every barcode in each nucleus or empty droplet from
529 single nucleus dissociation experiments, with magnified panel showing distribution from 0-200 UMIs on right
530 (median=1 in both real nuclei and empty droplets, indicated by arrowheads; n=157,073 nuclei:barcode
531 combinations, n=239,338 empty droplet:barcode combinations). **G.** Distribution of total barcode UMI transcripts
532 detected per nucleus or empty droplet (median=116 in real nuclei, median=1 in empty droplets, indicated by
533 arrowheads; n=1,307 nuclei, n=196,934 empty droplets). **H.** Number of unique barcodes detected per nucleus
534 or empty droplet (median=100 in real nuclei, median=1 in empty droplets; n=1,307 nuclei, n=196,934 empty
535 droplets). **I.** Number of UMI transcripts per each barcode, total barcode UMI transcripts, and unique barcodes
536 per nucleus or empty droplet. Box plot shows median and IQR of data in **(F–H)**. **J.** Stacked bar plot showing
537 fraction of barcodes uniquely found in empty droplets, nuclei, or both groups after implementing the indicated
538 UMI threshold. Percent of RVdG barcodes, nuclei, and empty droplets retained after implementing the UMI
539 threshold is overlaid. In **(D)** and **(I)**, p-values are computed using the Wilcoxon rank-sum test, *p<0.05.

540



541

542

543

544

545

546

547

548

549

Figure 8. Barcoded RVdG circuit mapping reveals the emergence of cell type-specific connectivity motifs in second trimester human cerebral cortex. **A.** Schematic of connectivity analysis. **B.** Number of starter cells per barcode network. **C.** Distribution of total number of cells per single-starter barcode network. **D.** Frequency of barcode networks containing different numbers of cells. Cell type proportions for each network size interval are indicated by color. **E.** Proportions of cell types in different barcode network size intervals. **F.** Example graph network showing the merged networks in one tissue slice infected with CVS-N2c RVdG. **G.** Sankey diagram showing observed connections by cell type (n=4,331 connections). **H.** Normalized connectivity matrix showing enrichment scores of observed connections compared to a random connectivity matrix

550 weighted by starter and uninfected cell type proportions (STAR Methods). P-values are computed using the
551 two-sided binomial tests with Bonferroni correction for multiple comparisons; * $p < 0.05$.

552

553

554 **STAR★METHODS**

555 **KEY RESOURCE TABLE**

556

REAGENT or RESOURCE	SOURCE	IDENTIFIER
Antibodies		
NeuN (chicken, 1:500)	MilliporeSigma	ABN91
NeuN (guinea pig, 1:500)	MilliporeSigma	ABN90
VGLuT1 (mouse, 1:200)	MilliporeSigma	MAB5502
PSD-95 (rabbit, 1:350)	Invitrogen	51-6900
SYP (guinea pig, 1:1000)	Synaptic Systems	101004
GFP (chicken, 1:1000)	Aves	1020
dsRed (rabbit, 1:250)	Takara	632496
RFP (rat, 1:250)	Chromotek	5F8
DLX2 (mouse, 1:50)	Santa Cruz	sc-393879
NEUROD2 (rabbit, 1:250)	Abcam	ab104430
Bacterial and Viral Strains		
5-alpha Competent E. Coli	New England BioLabs	C2987H
NEB Stable Competent E. Coli	New England Biolabs	C3040H
Stellar™ Competent Cells	Clontech Labs	636763
MegaX DH10B T1 ^R Electrocomp™ Cells	Thermo Fisher	C640003
Chemicals, Peptides, and Recombinant Proteins		
Heat-inactivated FBS	HyClone	SH30071.03HI
DMEM with Glutamax	Gibco	10569044
0.25% Trypsin-EDTA	Gibco	25200114
Poly-D-Lysine	MilliporeSigma	P7280
Polybrene	MilliporeSigma	TR-1003-G
Trans-Isrib	Tocris	5284

Chroman 1	Medchem Express	HY-15392
Emricasan	Selleckchem	S7775
Polyamine Supplement	Sigma-Aldrich	P8483
Glutamax	Gibco	35050-061
N2 supplement	Gibco	17502-048
B27 w/ Vitamin A	Gibco	17504-001
Neurobasal	Gibco	21103049
DMEM/F12 with Glutamax	Gibco	10565042
L-Ascorbic Acid 2-Phosphate	Wako Chemicals USA	321-44823
Non-essential amino acids	Gibco	11140050
Primocin	Fisher Scientific	NC9141851
Donkey Serum	Jackson Immuno	017-000-121
Prolong Gold	ThermoFisher	P36934
Fluoromount-G	ThermoFisher	00-4959-52
PEG8000	Promega	V3011
Sodium Chloride	Spectrum Chemical	SO160
1X PBS	Gibco	10010023
Trizol	ThermoFisher	15596026
Chloroform	Fisher Scientific	60-047-878
Phenol:Chloroform:Isoamyl Alcohol (25:24:1, v/v)	ThermoFisher	15593031
Glycoblue	ThermoFisher	AM9515
Ethanol, 200 proof	Weill Chem Central	TX89125-172SFU
Isopropyl Alcohol	Millipore Sigma	563935
Sodium Acetate, 3M	ThermoFisher	J61928.AE
Lipofectamine 3000	ThermoFisher	L3000015
Lipofectamine 2000	ThermoFisher	11668019

XFect	Takara	631318
XtremeGene HP	Roche	06366236001
FuGENE HD	Promega	E2311
PEI MAX	PolySciences	49553-93-7
TransIT-293	Mirus Bio	MIR2704
Q5 HotStart 2X Master Mix	New England BioLabs	M0494L
KAPA HotStart ReadyMix 2X	Fisher Scientific	NC0295239
EBSS	Worthington	LK003188
DNase I	MilliporeSigma	DN25-1 G
Trehalose	MilliporeSigma	T9531-25G
Potassium Chloride	MilliporeSigma	529552-1KG
Sodium Phosphate Monobasic	MilliporeSigma	S0751-1KG
Sodium Bicarbonate	MilliporeSigma	S5761-1KG
Glucose	MilliporeSigma	G7021-1KG
Magnesium Chloride Solution	MilliporeSigma	M1028-100ML
Calcium Chloride Solution	MilliporeSigma	21115-100ML
Potassium Gluconate	MilliporeSigma	P1847-100G
HEPES Solution	MilliporeSigma	H0887-100ML
Adenosine 5'-triphosphate Magnesium Salt	MilliporeSigma	A9187-100MG
Guanosine 5'-triphosphate Sodium Salt	MilliporeSigma	G8877-10MG
Sodium Phosphocreatine	MilliporeSigma	P7936-1G
Biocytin	MilliporeSigma	B4261-50MG
Potassium Hydroxide Solution	MilliporeSigma	P4494-50ML
EGTA	MilliporeSigma	E3889-100G
Recombinant RNase Inhibitor	Roche	09537589103
Critical Commercial Assays		
PIPseq T2 v4.0PLUS	Fluent Biosciences	FBS-SCR-T2-8-V4.05-FLU

Deposited Data		
scRNA-seq/snRNA-seq datasets	Raw: dbGAP Processed: UCSC Cell Browser	Raw: In Submission Processed: https://barcoded-rabies-cortex.cells.ucsc.edu
Barcoded RVdG Genome Library Sequencing Datasets	GEO	GSE277536
Experimental Models: Cell Lines		
LentiX 293T	Takara	632180
HEK-GT	Ben-Simon Lab	https://elifesciences.org/articles/79848
BHK-EnvA-TVA	Ben-Simon Lab	https://elifesciences.org/articles/79848
BHK-EnvA	Callaway Lab	Salk Institute Virus Core: BHK-EnvA
Neuro2A	ATCC	CCL-131
293T-TVA800	Callaway Lab	Salk Institute Virus Core: 293T-TVA800
Oligonucleotides: see Table S2		
Recombinant DNA		
pMD2.G	Addgene	12259
psPAX2	Addgene	12260
pcDNA 3.1 puro Nodamura B2	Addgene	17228
Barcoded SAD B19 RVdG dTomato genome plasmid	This Study	Will be submitted to Addgene
Barcoded CVS-N2c RVdG MCP- oScarlet-KASH genome plasmid	This Study	Will be submitted to Addgene
pCAG-B19N	Addgene	59924
pCAG-B19P	Addgene	59925
pCAG-B19G	Addgene	59921
pCAG-B19L	This Study	59922
pCAGGS-T7opt	This Study	65974

pSicoFlipped-syn-GFP-TVA-oG-WPRE-bGHpA	This Study	Will be submitted to Addgene
pSicoFlipped-syn-GFP-TVA-WPRE-bGHpA	This Study	Will be submitted to Addgene
pSicoFlipped-syn-GFP-TVA-oG-6xMS2-WPRE-bGHpA	This Study	Will be submitted to Addgene
Software and Algorithms		
ImageJ (Fiji)	ImageJ	https://imagej.net/Fiji
pClamp v11	Molecular Devices	https://www.moleculardevices.com/products/axon-patch-clamp-system/acquisition-and-analysis-software/pclamp-software-suite
PipSeeker v3.3	Fluent Biosciences	https://www.fluentbio.com/products/pipseeker-software-for-data-analysis/
R v4.3.3	R	https://www.r-project.org/
Python v3.11.4	Python	https://www.python.org/
JupyterLab v4.0.2	Project Jupyter	https://jupyter.org/
RStudio v2023.06.0+421	Posit	https://posit.co/download/rstudio-desktop/
Seurat v5.0	Satija Lab	https://satijalab.org/seurat/
Devtools v2.4.5	RStudio	https://devtools.r-lib.org/
BiocManager v1.30.23	Martin Morgan	https://bioconductor.github.io/BiocManager/
SeuratObject v5.0.2	Satija Lab	https://github.com/satijalab/seurat-object
dplyr v1.1.4	TidyVerse	https://dplyr.tidyverse.org
Ggplot2 v3.5.1	TidyVerse	https://ggplot2.tidyverse.org
EnhancedVolcano v1.20.0	Kevin Blighe	https://github.com/kevinblighe/EnhancedVolcano

harmony v1.2.0	Raychaudhuri Lab	https://github.com/immunogenomics/harmony
UCell v2.6.2	Carmona Lab	https://github.com/carmonalab/UCell
clusterProfiler v4.10.1	Yu Lab	https://github.com/YuLab-SMU/clusterProfiler
Msigdb v7.5.1	Igor Dolgalev	https://igordot.github.io/msigdb/
pandas v2.1.4	pandas Development Team	https://pandas.pydata.org/
NumPy v1.26.2	NumPy	https://numpy.org/
Matplotlib v3.8.2	Matplotlib Development Team	https://matplotlib.org/
SciPy v1.11.1	SciPy	https://scipy.org/
seaborn v0.12.2	Michael Waskom	https://seaborn.pydata.org/
statsmodels v0.14.3	statsmodels	https://www.statsmodels.org/stable/index.html
NetworkX v3.3	NetworkX Developers	https://networkx.org/
graphviz v0.20.3	graphviz Developers	https://pypi.org/project/graphviz/#description
SankeyMATIC	Steve Bogart	https://sankeymatic.com/build/
Affinity Designer	Affinity	https://affinity.serif.com/en-us/designer/
BioRender	BioRender	https://biorender.com/

Bowtie2 v2.5.1	Bowtie2	https://bowtie-bio.sourceforge.net/bowtie2/index.shtml
STAR v2.5.3a	https://sourceforge.net/projects/bbmap/	https://github.com/alexdobin/STAR/
BBMap v39.01	JGI BBTools	https://sourceforge.net/projects/bbmap/
UMI-tools v1.1.4	CGAT	https://github.com/CGATOxford/UMI-tools
Easy Electrophysiology	Easy Electrophysiology Ltd.	https://www.easyelectrophysiology.com/
Other		
Cell Culture Inserts, 0.4 µm pore size	MilliporeSigma	PICM03050
Dounce	Wheaton	EW-04468-00
Leica Widefield-Thunder Imaging System	Leica	UCSF Weill Microscopy Core
Leica SP8 Confocal Microscope	Leica	Nowakowski Lab
NextSeq 2000	Illumina	Canzio Lab, UCSF
NovaSeq X	Illumina	UCSF Center for Advanced Technology
FACSAria Fusion	BD Biosciences	UCSF Laboratory for Cell Analysis
BX51WI Microscope	Olympus	BX51WI
6-8 MΩ Resistance Glass Microelectrodes	Sutter Instruments	BF150-86-10
Multiclamp 700B Amplifier	Molecular Devices	700B
Digidata 1550B	Molecular Devices	1550B

557
558

RESOURCE AVAILABILITY

559

Materials Availability

560 Plasmids generated in this study will be made available through Addgene. Other reagents are available from
561 the Lead Contact, Dr. Tomasz Nowakowski (tomasz.nowakowski@ucsf.edu), upon reasonable request.

562 **Data and Code Availability**

563 scRNA-seq and snRNA-seq raw data will be made available through dbGAP, and processed data are available
564 through the UCSC Cell Browser: <https://barcoded-rabies-cortex.cells.ucsc.edu>. Sequencing data from
565 barcoded viral genome and plasmid libraries for assessing diversity is available through GEO (GSE277536,
566 private token: craxaqkirzkrtit). Other data that support the findings of this study are available from the Lead
567 Contact, Dr. Tomasz Nowakowski (tomasz.nowakowski@ucsf.edu) upon reasonable request. All code used for
568 analysis has been deposited at Github and will be publicly available as of the date of publication.

569 **EXPERIMENTAL MODEL AND SUBJECT DETAILS**

570 **Human Primary Cerebral Cortex Specimens**

571 De-identified tissue samples were collected with previous patient consent in strict observance of the legal and
572 institutional ethical regulations. Protocols were approved by the Human Gamete, Embryo, and Stem Cell
573 Research Committee (Institutional Review Board) at the University of California, San Francisco.

574 **METHOD DETAILS**

576 **Generation of lentiviral helper plasmid and barcoded RVdG plasmid library**

577 We cloned a lentiviral helper plasmid in which the human synapsin I promoter (hSyn1) drove the expression of
578 a human codon-optimized GFP, TVA, and chimeric glycoprotein oG¹⁸ (pSico-hSyn1::GFP-T2A-TVA-E2A-oG).
579 A modified pSico plasmid¹¹ was utilized as the backbone, and the sequence between the cPPT/CTS and 3'
580 LTR was replaced with DNA fragments containing the hSyn1 promoter and human codon-optimized
581 sequences GFP, T2A, TVA, E2A, and oG via gibson assembly using HiFi DNA Assembly Master Mix (NEB,
582 E2621).

583 To prepare a SAD B19 strain rabies genome plasmid for barcoding (pSADdeltaG-dTomato), the
584 pSADdeltaG-BFP plasmid (Addgene #32639) was digested with NheI-HF (NEB, R3131) and AscI (NEB,

R0558) to replace the gene encoding tagBFP2 with a gblock (IDT) containing a gene encoding a human codon-optimized dTomato and a barcode cloning site in the 3' UTR of dTomato represented by two SacII restriction enzyme sites. To generate the backbone for the barcoded plasmid library, 10 µg of pSADdeltaG-dTomato was digested using SacII (NEB, R0157) overnight and purified using the Zymo DNA Clean and Concentrator-5 kit (Zymo, D4004). The insert containing the barcode library was generated by performing PCR on the STICR barcoded lentiviral plasmid library¹¹ (Addgene 180483) using primers flanking the barcode sequences and containing overhangs matching the SacII-digested pSADdeltaG-dTomato plasmid (Primers 1 and 2, [Table S2](#)).

Similarly, to prepare a CVS-N2c strain rabies genome plasmid for barcoding and nuclear capture, the RabV CVS-N2c(deltaG)-mCherry plasmid (Addgene #73464) was digested with SmaI (NEB, R0141) and NheII-HF (NEB, R3131) to replace the gene encoding mCherry with a gblock (IDT) encoding a fusion protein consisting of the MS2 coat protein MCP, the fluorescent protein oScarlet, and the KASH nuclear localization signal. The 3' UTR of this gblock carried six MS2 hairpin sequences followed by a barcode cloning site represented by two SacII restriction enzyme sites. 10 µg of the resulting plasmid was digested using SacII (NEB, R0157) overnight and purified using the Zymo DNA Clean and Concentrator-5 kit (Zymo, D4004). The insert containing the barcode library was generated by performing PCR on the STICR barcoded lentiviral plasmid library¹¹ (Addgene 180483), with overhangs matching the SacII digested plasmid (Primers 1 and 2, [Table S2](#)).

Based on our initial qPCR optimization (Figure S1C), 10 cycles of PCR were performed on 25 ng of plasmid DNA in 50 µL total volume using KAPA HotStart PCR ReadyMix (Roche KK2601), with the following parameters: Initial denaturation: 95C for 3 min, Denaturation: 98C for 20 s, Annealing: 62C for 15 s, Extension: 72C for 10 s. A total of 5 PCR reactions was performed, which represents a starting amount of approximately 1.3×10^{10} molecules of DNA, or ~100-fold excess of the theoretical diversity of the plasmid library. Each PCR reaction was subsequently supplemented with 5 µL of CutSmart Buffer (NEB B7204) and digested using 1 µL DpnI restriction enzyme (NEB R0176) to eliminate plasmid DNA. Fragments were eluted using the Zymo DNA Clean and Concentrator-5 Kit.

611 To generate the barcoded rabies plasmid library for both SAD B19 and CVS-N2c strains, 12 20- μ L
612 reactions of gibson assembly were performed for 1 hour at 50C using the HiFi DNA Assembly MasterMix
613 (NEB, E2621), with each reaction containing 184.9 ng of SacII-digested plasmid and a 10-fold molar excess of
614 PCR-amplified insert. The 12 gibson assembly reactions together contain $\sim 1.3 \times 10^{11}$ molecules of digested
615 backbone, which is 1000-fold excess to the theoretical complexity of 125 million. The gibson assembly
616 reactions were pooled and purified using Zymo Clean and Concentrator-5 Kit in 12 μ L of nuclease-free water
617 pre-heated to 70C. After cooling on ice, the purified gibson assembly reaction was transformed into a total of
618 300 μ L of MegaX DH10B Electrocompetent E. Coli (Thermo, C640003) and grown overnight at 37C in LB-
619 Carbenicillin broth. Some of the transformed bacteria were also plated at $1:1 \times 10^4$, $1:1 \times 10^5$, and $1:1 \times 10^6$
620 dilution on LB-Agar-Carbenicillin plates, to estimate the total number of colonies to verify sufficient diversity.
621 The following day, LB-containing bacteria were spun down at 4500xg for 15 min and plasmid DNA was
622 extracted in AE buffer using the Nucleobond 10000 EF Giga Kit (Machery Nagel, 740548) or the ZymoPure II
623 Plasmid GigaPrep Kit (Zymo D4204).

624 **Generation of barcoded RVdG viral libraries**

625 For library Replicates 1-4 (Figure 1), five 15 cm dishes were coated with 10 μ g/mL poly-D-lysine (PDL) diluted
626 in 1x PBS for 1 h at room temperature, and rinsed three times with PBS. Lenti-X HEK293T or HEK-GT¹⁷ cells
627 that were 70-80% confluent were dissociated using 0.05% Trypsin-EDTA (Thermo, 25200056) and 13 million
628 cells were plated into each PDL-coated 15-cm dish in “FBS-DMEM media”, which was composed of DMEM
629 (Thermo, 41966) containing 10% Heat-inactivated FBS (HI-FBS, Cytiva, SH30071.03HI) and 2% primocin
630 (Invivogen, ant-pm-1). The next day, when the cells had reached $\sim 90\%$ confluence, each 15 cm dish was
631 transfected with 27.1 μ g of SAD B19-N (Addgene #32630), 13.9 μ g of SAD B19-P (Addgene #32631), 13.9 μ g
632 of SAD B19-L (Addgene #32632), 16.6 μ g of CAGGS-T7opt (Addgene #65974), and either 55.1 μ g of
633 barcoded pSADdeltaG-dTomato (Libraries 1-2) or pCVS-N2c(deltaG)-MCP-oScarlet-KASH-6XMS2 (Libraries
634 3-4), using Lipofectamine 3000 (Thermo, L3000075) following the manufacturer’s recommendations. In
635 addition, the Lenti-X HEK293T was co-transfected with 11 μ g of SAD B19-G (Addgene #32633). For every
636 microgram of plasmid, 2 μ L of P3000 reagent and 2.33 μ L of Lipofectamine 3000 was used. The day following
637

transfection, cells were passaged into PDL-coated plates at a 1.28:1 ratio based on surface area (i.e. one 15 cm dish into two 10 cm dishes) using FBS-DMEM media that was additionally supplemented with 1 CEPT cocktail⁸⁷ (50 nM Chroman 1, 5 μ M Emricasan, 0.7 μ M Trans-Isrib, 1 \times polyamine supplement). Media was replaced the next day with FBS-DMEM media containing CEPT. Viral supernatant was collected on the fourth, fifth, and sixth day post-transfection to harvest G-pseudotyped virus, with media replacement using FBS-DMEM media containing CEPT. Viral supernatant was collected and filtered through a 0.45 μ m syringe filter (Corning 431220). Supernatant was concentrated using PEG precipitation with 1 volume of PEG concentrator for every 3 volumes of supernatant (PEG concentrator: 40% (w/v) PEG 8000 (Promega, V3011) in 1 \times PBS (Thermo, 10010023) supplemented with 1.2 M NaCl (Fisher, S271-500), and incubated overnight at 4C with gentle agitation. The next day, the precipitated viral particles were spun down by centrifugation at 1600xg for 1 hour at 4C. The supernatant was removed and the viral pellet was resuspended using FBS-DMEM media and 8 μ g/mL of polybrene (Millipore Sigma TR-1003-G) at 1:100 of the original media volume.

Per every mL of concentrated G-RVdG virus, 3 million BHK-EnvA-TVA cells¹⁷ (Library 1), BHK-EnvB cells (Library 2; Salk Institute Viral Core), or BHK-EnvA cells (Libraries 3 and 4; Salk Institute Viral Core) were transduced by spin-infection (1500xg, 1.5 hr, room temperature, using a swinging bucket rotor). Subsequently, cells were plated into 10 cm dishes at a density of 3 million cells/dish in FBS-DMEM media containing 8 μ g/mL of polybrene. The following day, the media was replaced with fresh media without polybrene. One or two days later, when the plate reached confluence, cells were passaged once more using 0.25% trypsin-EDTA for 10 minutes at 37C, in order to deactivate any residual G-pseudotyped virus. FBS-DMEM media was added to trypsinized cells at 3-fold volume excess to quench the trypsin, and cells were spun down to remove the trypsin-EDTA. Cells were pooled and passaged at a 1:2.5 dilution (i.e. one 10 cm dish into one 15 cm dish). Cells were given a media change the next day. Two days later, when plates had reached confluence, viral supernatant was collected every other day for a total of 3-4 collections, depending on the health of the cells. On the day of collection, viral supernatant was filtered through a 0.45 μ m syringe filter and concentrated by ultracentrifuge (Beckman Coulter) through a 4 mL sucrose cushion using the SW32Ti rotor (20,300 RPM, 2 hr, 4C). After ultracentrifugation, the viral pellet was resuspended in 50 μ L of HBSS while gently rocking overnight at 4C. Virus was aliquoted, frozen at -80C, and titered by infecting TVA800 HEK293T cells (Salk Institute Viral

665 Core) using a serial dilution of virus, and measuring the percentage of dTomato-positive cells two days later by
666 flow cytometry. Titers typically ranged from between 10^7 - 10^8 TU/mL, and lack of G-contamination was
667 confirmed by infecting 100,000 Lenti-X HEK293T cells (that do not express TVA) with 1 μ L of undiluted
668 barcoded RVdG virus.

669 **Testing the effect of cell lines and transfection reagents on RVdG viral rescue efficiency**

670 To compare rescue efficiency in different packaging cell lines, Lenti-X HEK293T cells, BHK-21, and Neuro2A
671 cells were passaged into PDL-coated 24-well plates as described above at a density of 1.75×10^5 cells per
672 well (HEK293T, Neuro2A) or 1.1×10^5 cells per well (BHK-21). The next day, when the cells had reached
673 ~90% confluence, each well was transfected with 760 ng of barcoded pSADdeltaG-dTomato, 374 ng of SAD
674 B19-N, 192 ng of SAD B19-P, 192 ng of SAD B19-L, and 229 ng of CAGGS-T7opt using Lipofectamine 3000
675 following manufacturer recommendations. For every μ g of DNA, 2 μ L of P3000 reagent and 2.33 μ L of
676 Lipofectamine 3000 were used. The next day, the media was changed with fresh FBS-DMEM media. Two days
677 later, cells were dissociated using 0.05% Trypsin-EDTA, quenched with three volumes of FBS-DMEM media
678 for every one volume of Trypsin-EDTA, and pelleted by centrifugation at 300xg for 3 minutes. Cells were
679 resuspended using 1x PBS containing 0.1% bovine serum albumin (BSA) and filtered into a flow cytometry
680 tube through a 35 μ m nylon mesh cap. Flow cytometry was performed while recording from 50,000 events to
681 quantify the percentage of cells that had successfully recovered RVdG viral particles based on dTomato
682 expression.
683

684 To compare rescue efficiency in HEK293T comparing different transfection reagents, Lenti-X HEK293T
685 cells were passaged into PDL-coated 24-well plates as described above, and transfected using Lipofectamine
686 3000 as described above, Lipofectamine 2000 following published recommendations¹⁴ (1.17 μ L per 1 μ g of
687 DNA), Xfect following published recommendations⁴ (0.3 μ L per 1 μ g of DNA), FuGENE HD (3 μ L per 1 μ g of
688 DNA), PEI MAX (3 μ L per 1 μ g of DNA), XtremeGene HP (3 μ L per 1 μ g of DNA), and Mirus TransIT-293 (3 μ L
689 per 1 μ g of DNA). Media was changed the next day and flow cytometry was performed three days after
690 transfection.
691

Production of barcoded RVdG for comparison of transfection reagents, plate size, and cell lines

To compare the effect of packaging RVdG using Lipofectamine 2000 in HEK293T cells, Lipofectamine 3000 in HEK293T cells, and Lipofectamine 3000 in HEK-GT cells on RVdG viral library complexity, eight PDL-coated 15-cm dishes were plated with Lenti-X HEK293T cells and four PDL-coated 15-cm dishes were plated with HEK-GT cells as described above. Each dish functioned as a technical replicate for this experiment. Each 15 cm dish was transfected with 55.1 μg of barcoded CVS-N2c MCP-oScarlet-KASH, 27.1 of SAD B19-N, 13.9 μg of SAD B19-P, 13.9 μg of SAD B19-L, and 16.6 μg of CAGGS-T7opt using Lipofectamine 3000 or Lipofectamine 2000 as described above. Transfection of HEK293T, but not HEK-GT cells additionally included 11 μg of SAD B19-G. The next day, the contents of each 15 cm dish were passaged using 0.05% Trypsin-EDTA into two 10-cm dishes, while keeping cells from each 15 dish separate. Media was changed the next day, and supernatant was collected to harvest G-pseudotyped RVdG when approximately half of the cells were oScarlet-positive (day 5 post-transfection for Lipofectamine 3000 in HEK293T and HEK-GT cells, day 8 post-transfection for Lipofectamine 2000). The supernatant from the 10-cm dishes that originated from the same 15-cm dish were pooled and concentrated using PEG precipitation, and viral genome RNA was isolated as described in the next section.

To compare the effect of packaging RVdG in 10-cm dishes and 384 well plates, two PDL-coated 15-cm dishes containing LentiX HEK293T cells were transfected with packaging plasmids as described above. The next day, cells from one 15-cm dish were passaged into two PDL-coated 10-cm dishes, and cells from the other 15-cm dish were passaged into five PDL-coated 384 well plates. Media was changed the next day and supernatant was harvested four days post-transfection for concentration and viral genome RNA isolation as described in the next section.

Generation of sequencing library for plasmid and viral barcode diversity quantification

To quantify plasmid barcode library diversity, 50 ng of plasmid DNA was tagmented using seqWell's Tagify UMI reagent, in order to tag each barcode-containing plasmid DNA fragment with a UMI and partial Illumina Read1 adapter. Tagmented fragments were purified using a 1 \times left-sided size selection using SPRIselect beads according to the manufacturer's protocol. Sample indexing PCR was subsequently performed using

719 custom sample index primers that bind to the TruSeq P5 PCR handle generated during Tn5 tagmentation
720 (Primer 3, [Table S2](#)) and to the BFP primer site sequence immediately proximal to the barcode sequence
721 (Primers 8-15, [Table S2](#)). The library was sequenced using a target of 100 million reads.

722 To quantify viral barcode library diversity, barcoded RVdG from a single 15 cm dish was concentrated
723 by ultracentrifugation or PEG precipitation as described above and RNA was isolated by phenol-chloroform
724 extraction, the procedure for which is described as follows. The viral pellet was resuspended in 1 mL of Trizol
725 (Invitrogen 15596026), and incubated at room temperature for five minutes to permit dissociation of rabies
726 proteins from viral RNA. Subsequently, 200 μ L of chloroform (Fisher 60047878) was added and vortexed for
727 30 seconds, followed by spin at 12000 \times g for 15 min at 4C. 600 μ L of the upper aqueous phase was collected
728 and RNA was precipitated by mixing with 500 μ L of isopropanol and 1 μ L of Glycoblue (Invitrogen AM9515)
729 and incubating for 10 minutes. Precipitated RNA was pelleted by centrifugation at 12000 \times g for 10 min at 4C,
730 washed twice with 80% ethanol, air dried for 2 min, and resuspended in 10 μ L of nuclease-free water. Reverse
731 transcription was performed on 1-5 μ g of RNA using SuperScript IV (ThermoFisher 18090010) and 1 μ L of 50
732 mM custom RT primer (Primer 4, [Table S2](#)) targeting a sequence distal to the barcode relative to the negative
733 stranded viral genome, in order to generate cDNA containing barcodes from viral genome RNA but not from
734 contaminant mRNA. RT primer also contained an overhanging sequence carrying an 8 bp randomer, which
735 functions as a UMI to correct for PCR amplification bias after sequencing, and a binding site for Illumina
736 sample index primer. The resulting cDNA (5 μ L, or 25% of the RT reaction) was amplified using 10-12 cycles of
737 PCR with KAPA HotStart PCR ReadyMix (Roche KK2601) and custom sample index primers (P7 primers:
738 Primers 5-7; P5 primers: Primers 16-23; [Table S2](#)), one of which is specific to an overhang introduced by the
739 RT primer to facilitate viral genome-specific amplification. Each library was sequenced using at least 10 million
740 reads.

741 **Organotypic slice culture and viral transduction of human brain**

742 To generate organotypic slice cultures, cortical tissue was identified by visual inspection, embedded in 3% low
743 melting point agarose (Fisher, # BP165–25), and sliced into 300 μ m sections perpendicular to the ventricle
744 using a Leica VT1200S vibrating blade microtome. Slicing was performed in oxygenated artificial cerebrospinal
745

746 fluid (ACSF) containing 125 mM NaCl, 2.5 mM KCl, 1 mM MgCl₂, 1 mM CaCl₂, 1.25 mM NaH₂PO₄. Slices were
747 cultured on Millicell Standing Cell Culture Inserts (PICM03050) in a serum-free media composed of DMEM-F12
748 with Glutamax (Gibco 10565018) and Neurobasal media (Gibco 21103049) mixed at a 1:1 (v/v) ratio and
749 supplemented with 2% B27 (Gibco 17504044), 1% N2 (Gibco 17502048), 200 μM ascorbic acid-2-phosphate
750 (Wako 50-990-141), and 2% primocin. One hour after plating, slices were transduced with a VSV-G
751 pseudotyped lentiviral helper virus (pSico-hSyn1::GFP-T2A-TVA-E2A-oG) described above by pipetting 2 μL of
752 10⁶ TU/mL over the top of the slice. Half of the media was exchanged every other day subsequently. Slices
753 were transduced with barcoded RVdG-dTomato by pipetting 3 uL of 10⁷ TU/mL virus over the top of the slice
754 three days after the initial helper virus infection. Five days after transduction with RVdG-dTomato, slices were
755 dissociated into a single cell or single nuclei suspension following previously published protocols^{88,89}. For single
756 cell dissociation, 100 units of papain in 1 mM L-cysteine and 0.5 mM EDTA were reconstituted in 5 mL of
757 EBSS containing 5% Trehalose and reactivated for 10 minutes. 500 units of DNase I was added to 5 mL of
758 reactivated papain solution and slices were incubated in 1 mL of papain/slice for 30 min at 37C. Papain was
759 subsequently inactivated using EBSS containing 58.3% ovomucoid inhibitor, 5% DNase I, and 5% Trehalose
760 (EBSS-ovomucoid), using a 1:1 (v/v) papain:EBSS-ovomucoid inhibitor ratio. Slices were spun down at 100×g
761 for 10 min at 4C, resuspended in 1 mL of EBSS-ovomucoid, and gently triturated 30 times using a fire-polished
762 glass pipette, or until the tissue has been fully dissociated into a single cell suspension. 4 mL of PBS
763 containing 1% BSA, 5% Trehalose, and 5% DNase I was added per 1 mL of EBSS-ovomucoid, mixed gently,
764 and spun down at 100×g for 10 min at 4C. Cells were resuspended in ice-cold PBS containing 1% BSA and
765 filtered through a 35 μm strainer mesh in preparation for fluorescence-activated cell sorting (FACS).

766 For single nuclei dissociation, slices were placed in a pre-chilled 1 mL dounce homogenizer (Wheaton
767 EW-04468-00) and slowly dounced ten times with the loose pestle A and ten times with the tight dounce pestle
768 B while on ice using 1 mL EZ lysis buffer (Sigma NUC-101) supplemented with 5 μL of RNase inhibitor
769 (Takara 2313B; 40 U/uL). The contents of the dounce were moved to a pre-chilled 15 ml conical tube,
770 incubated for 5 min on ice, and spun down in a swinging bucket centrifuge at 4C, 500×g, for 5 min.
771 Supernatant was gently removed, and nuclei were gently resuspended in ice-cold 1 mL EZ lysis buffer
772 supplemented with 5 μL of RNase inhibitor using 3-5 triturations using a 1 mL pipet and normal-bore tips.

773 Nuclei were incubated for 5 min, spun down in a swinging bucket centrifuge at 4C, 500×g, for 5 min, and
774 resuspended in ice-cold PBS containing 1% BSA and filtered through a 35 µm strainer mesh in preparation for
775 fluorescence-activated nuclei sorting (FANS).

776 FACS/FANS was performed to isolate dTomato+ cells or oScarlet+ nuclei using a 100 µm or 85 µm
777 nozzle, respectively, on a BD FACSAria Fusion. Cells were collected in a PCR tube nested within a 600 µL
778 tube nested within a 1.5 mL Eppendorf tube⁹⁰ containing 50 µL of collection buffer consisting of PBS-1% BSA
779 and 200 units/mL RNase inhibitor. The PCR tube had previously been precoated with 1% BSA for one hour, to
780 prevent cells from sticking to the side of the tube during FACS/FANS. One final centrifugation was performed
781 to pellet the cells/nuclei (cells: 300×g for 5 min, nuclei: 500×g for 5 min), and the supernatant was carefully
782 removed to leave behind approximately 4 µL of collection buffer.

784 **Generation of transcriptome and barcode libraries**

785 scRNA-seq and snRNA-seq was performed on collected cells/nuclei using the PIPseq v4.0 T2 3' Single Cell
786 RNA kit, adhering to the manufacturer's protocol for isolating single-cell and single-nucleus transcriptomes.
787 Transcriptomes were sequenced with a target of 35,000 reads/cell.

788 For generating barcode libraries, PCR was performed on 25% of the cDNA amplification library using
789 custom sample index primers that target the BFP primer site immediately proximal to the barcodes (Primers 8-
790 15; [Table S2](#)) and the partial Illumina Read1 sequence introduced by the 10x RT primer (Primers 16-23; [Table](#)
791 [S2](#)). 10-15 rounds of PCR was performed using the following program: 1) 98C, 30s, 2) 98C, 10 sec, 3) 62C, 20
792 sec, 4) 72C, 10 sec, 5) Repeat steps 2–4 9-14×, 6) 72C, 2 min, 7) 4C, hold, as described previously¹¹. Barcode
793 library was purified by 0.6-1× dual-sided size selection using SPRIselect beads (Beckman Coulter B23317)
794 and sequenced with a target of 5,000-10,000 reads/cell using the following sequencing parameters: Read 1: ≥
795 54 reads, Index 1: 8 reads, Index 2: 8 reads, Read 2: 150 reads.

797 **Whole-cell patch-clamp recordings**

798 Electrophysiological experiments were conducted on cultured human prenatal subplate neurons at DIV 6-8 (i.e.
799 3-5 days after transduction with RVdG-dTomato). Cultured brain slices were placed in a recording chamber

800 mounted on a BX51WI microscope (Olympus) and were perfused with artificial cerebrospinal fluid (ACSF)
801 containing (in mM): 125 NaCl, 2.5 KCl, 1.25 Na H₂PO₄, 25 NaHCO₃, 11.1 Glucose, 1 MgCl₂, 2 CaCl₂, pH 7.4,
802 305-310 mOsm, equilibrated with 95% O₂, 5% CO₂ at 34 ± 1°C. Fluorescence imaging with a 40× water
803 immersion objective lens (LUMPLFLN40XW, NA 0.8) was used to identify starter and non-starter cells (GFP
804 and dTomato/oScarlet fluorescence together vs. dTomato/oScarlet fluorescence alone, respectively). Whole-
805 cell patch-clamp recordings were performed on fluorescently labeled cells using 6–8 MΩ resistance glass
806 microelectrodes (BF150-86-10; Sutter Instrument) containing an internal solution comprised of (in mM): 120 K
807 gluconate, 4 KCl, 10 HEPES, 4 MgATP, 0.3 Na₃GTP, 10 sodium phosphocreatine, 13.4 biocytin, pH 7.25 with
808 0.5M KOH, ~320 mOsm. In a subset of experiments, a slightly modified internal solution was used consisting
809 of (in mM): 111 K gluconate, 4 KCl, 10 HEPES, 0.2 EGTA, 4 MgATP, 0.3 Na₃GTP, 5 sodium phosphocreatine,
810 13.4 biocytin, pH 7.25 with 0.5M KOH with addition of 1 U/μl recombinant RNase inhibitor (Roche) immediately
811 prior to experiment and final osmolarity of 315–320 mOsm. All signals were obtained using Multiclamp 700B
812 amplifier and Digidata 1550B (Molecular Devices). Specifically, voltage-clamp recordings were sampled at 20
813 kHz, low-pass filtered at 2kHz, and current-clamp recordings were sampled at 50 kHz, low-pass filtered at 10
814 kHz. Easy Electrophysiology software (Easy Electrophysiology Ltd.) was used to analyze recorded traces that
815 met the following quality control criteria: (1) >1 GΩ seal before whole-cell configuration; (2) series resistance
816 <25 MΩ; and (3) <20% series resistance changes between before, during and after the recording. In current
817 clamp configuration, 1-s long current steps were injected ranging from -20 pA to 60 pA in 2 pA increments to
818 elicit action potentials. The resting membrane potential was measured as the mean membrane potential during
819 100 ms before the current stimulation. The input resistance was calculated as the voltage difference between
820 the steady state and the resting membrane potential divided by the injected current during the hyperpolarizing
821 steps. The cell membrane capacitance was measured as the time constant of a monoexponential fit to the first
822 local minimum of the hyperpolarizing membrane potential during stimulation divided by the membrane
823 resistance. Action potential was identified initially by locating the action potential threshold, which was defined
824 as the potential at which the first derivative of the membrane potential (dV/dt) exceeded 20 mV/ms. Only those
825 peaks with the following criteria were detected as an action potential: > 20 mV amplitude, > 20 mV/ms
826 upstroke, > -0.1 mV/ms downstroke, < 5 ms width.

827

828 **QUANTIFICATION AND STATISTICAL ANALYSIS**

829 Statistical analyses were performed in RStudio and Jupyter. Information regarding statistics including the
830 statistical test, sample sizes, and p-values for each experiment are provided in the figure legends and the
831 Results section. A p-value of less than 0.05 was considered statistically significant, with corrections applied for
832 multiple comparisons when necessary.

833

834 **Viral barcode pre-processing**

835 Output fastqs from sequenced rabies barcode libraries were filtered and processed using the custom script
836 `barcode_processing.sh`. The `bbduk`⁹¹ (v39.01) package (BBMap) was used to discard any reads with average
837 quality (maq) below 20. Reads were then trimmed down to individual RVdG barcodes, UMIs, and cell barcodes
838 (for transcriptome-matched datasets). RVdG barcodes were aligned to a custom reference white list ([Table S1](#))
839 with `bowtie2`, allowing for one base pair mismatch per read. After sorting output files with `samtools`, the RVdG
840 barcodes, UMIs, and cell barcodes were merged on read IDs. The command line package `UMI-tools`⁹² (v1.1.2)
841 was then used to quantify the number of UMIs per cell barcode and RVdG barcode combination. A UMI
842 collapsing threshold was set at 1 to collapse any UMIs with only one base pair difference into a single UMI
843 count.

844

845 **Viral barcode diversity analysis**

846 When available, UMI counts per RVdG barcode were retrieved from previously published studies³⁻⁵. For those
847 studies that were not already in the output format of `UMI-tools`, counts per barcode were generated using `UMI-`
848 `tools` from published barcode lists. Barcode library diversity was compared using the percentage of the UMIs
849 covered by each unique rabies barcode per dataset plotted with `Matplotlib`⁹³ (v3.9.1).

850

851 **Barcode collision simulations**

To evaluate the risk of barcode collision (or the chance of a cell receiving the same barcode as a previously infected cell), we set up a simulation in which 10-100,000 cells (for viral libraries) or 10-10,000,000 cells (for plasmid libraries) are assigned a single barcode by bootstrapping from the original dataset with replacement (Figures 1E, S1K, S1M, and S1O). Each simulation was repeated 50 times using `numpy.random.choice` in the Numpy⁹⁴ package, and duplicate barcodes were counted with the pandas⁹⁵ package's `pandas.dataframe.duplicated(keep=first)` command to ensure that barcode collision was counted starting from the first duplicate barcode infection. Barcode collision was then plotted as a function of the number of cells per simulation. Line plots showing the collision metric value at each of the starter cell counts were drawn using the Seaborn⁹⁶ (v0.12.2) package in Python with error bars extended to two standard error widths based on the results from the 50 iterations for each simulation.

Barcode sampling simulations

To examine the total number of unique barcode as a function of the number of transcripts sequenced, we set up a simulate in which 10-1,000,000 barcodes were pulled from barcode diversity datasets at random using `numpy.random.choice` in the Numpy⁹⁴ with replacement (Figure 1F). These simulations were repeated 100 times, and error was calculated as standard deviation. Line plots showing the total number of unique barcodes pulled versus the total number of all barcodes pulled were plotted using Matplotlib⁹³ (v3.9.1) with error bars extending to two standard error widths based on the results from the 100 iterations for each simulation.

Shannon entropy calculations

To estimate the Shannon entropy for the libraries presented and previous published ones, the function `shannon_entropy_calculator()` was created. Iterating through a list of barcode libraries, it computes the observed barcode probability distributions by dividing the UMI count of a barcode by the sum of UMI counts in the library. Uniform barcode probability distributions are calculated by specifying each barcode probability as 1 divided by the sum of UMI counts in the library. The probability distributions are inputted into the SciPy `entropy()` function to calculate the observed and uniform Shannon entropies (in bits) for each library.

879

880 **Transcriptomic processing and analysis**

881 Output fastqs from PIPseq datasets were first aligned using the PIPseeker³ (v3.3) prebundled hg38 genome to
882 generate mitochondrial gene counts and complete cell barcodes. The argument `-retain-barcoded-fastqs`
883 was used to retain original fastqs with modified cell barcodes. These fastqs were then concatenated per
884 dataset and realigned with STAR (v2.7.11b) to the hg38 reference genome with NCBIRefSeq annotations to
885 generate transcriptomic count matrices. Filtered matrices with the lowest sensitivity were processed using
886 Seurat (v4.3)⁹⁷. Briefly, single-cell datasets were filtered for cells with >1000 features, >1250 UMI counts, and
887 <5% mitochondrial genes. Single-nuclei datasets were filtered for nuclei with >300 features, >300 UMI counts,
888 and <5% mitochondrial genes. To identify cell types, all datasets were merged and normalized using
889 `SCTransform()`. The top 2000 variable features were selected, and mitochondrial genes were regressed out
890 from further analysis. PCA was calculated using the top 50 principal components of the SCT assay. The
891 package Harmony²² (v1.2.0) was then used to integrate all datasets to account for batch effects and
892 differences between dissociation methods. `RunUMAP()`, `FindNeighbors()`, and `FindClusters()` were used to
893 cluster the resultant object, accounting for dimensions 1:40 with cluster resolution set to 1.0. Marker genes
894 across clusters were identified using the package presto⁹⁸ (v1.0.0) and Seurat's `FindAllMarkers()` function.
895 Cell type labels were identified based on expression of key marker genes. These cell type labels were retained
896 for all downstream analyses.

897

898 **Gene set enrichment analysis**

899 To identify differentially expressed genes between the uninfected, SAD B19-, and CVS-infected datasets
900 dissociated as single-cells, these datasets were merged and then processed using the same parameters
901 described above, excluding integration with Harmony. Differentially expressed genes between uninfected, SAD
902 B19-, and CVS-infected datasets and each cell type were identified using Seurat's `FindMarkers()` function.
903 Top differentially expressed genes were visualized using the EnhancedVolcano⁹⁹ (v1.20.0) package. Gene set
904 enrichment analysis was conducted using the `gseGO()` function in clusterProfiler^{100,101} (v4.10.1) and restricted
905 to the Gene Ontology's Biological Processes database. FDR adjusted p-values were reported, and the top ten

906 pathways with an adjusted p-value <0.05 were visualized using the `dotplot()` function. Cell type-specific
907 enrichment of certain terms was confirmed by calculating term enrichment per cell using the
908 `AddModuleScore_UCell()` function in the `UCell`¹⁰² package (v2.6.2), then mapping enrichment scores using
909 Seurat's `FeaturePlot()` function.

911 **Nuclear and cellular viral barcode metric comparisons**

912 Medians and distributions of UMI counts for every unique rabies barcode found in every unique cell/nucleus, as
913 well as the total number of rabies barcode UMIs per every unique cell/nucleus were plotted using Matplotlib
914 (v3.9). The relationship between total rabies barcode UMIs and total unique rabies barcode per cell/nucleus
915 and lines of best fit were plotted with seaborn (v0.13.2). R^2 was calculated by squaring the Spearman's
916 Correlation coefficients calculated using SciPy's (v1.11.1) `spearmanr()` function.

918 **Empty droplet analysis**

919 Cell/nucleus barcodes representing empty droplets were identified from Pipeseeker's generated barcode read
920 info table as any cell barcode with ≤ 10 transcripts mapping to the hg38 reference genome. All rabies barcodes
921 with cell/nucleus barcodes matching those corresponding to empty droplets were considered for empty droplet
922 analysis. The distribution and central tendencies of UMIs per rabies barcode per cell/nucleus or empty droplet,
923 total rabies barcode transcripts, and unique rabies barcode identified across either real cells/nuclei or empty
924 droplets were calculated and visualized using SciPy's¹⁰³ (v1.11.1) `ranksums()` function with Bonferroni
925 correction and Matplotlib packages. Fractions of barcodes in empty droplets, cells/nuclei, or both were
926 visualized using ggplot2 (v3.5.1).

928 **Preparing barcode data for connectivity analysis**

Barcode data was prepared for connectivity analysis using the function `process_barcodes_df()` written in Python (Table S4). This filtered for cells that passed QC, and annotated each RVdG barcode-cell/nucleus barcode (CBC) based on the CBC's cell type and number of helper UMIs. Barcode and helper UMI thresholds of ≥ 3 were used to filter for barcodes and assign starter status. Additional annotations were made for barcodes that were found in at least 2 cells; whether the barcode was found in starter cells, non-starters, or both; and whether the barcode was only found in one starter cell (termed "single_starter_barcodes").

Identification of single-starter networks

To systematically infer single-starter networks involving a single starter cell and all of the non-starter cells that share at least one one barcode with the starter, we filtered the dataset generated using the function `process_barcodes_df()` for single starter barcodes that were found in at least one nonstarter cell. All of such barcodes associated with a cell were grouped into a set for each cell. Iterating through each starter cell's barcode set and all of the non-starter cell's barcode sets, non-starters that shared at least one barcode with a given starter cell (as determined by the intersection of their sets being >0) were matched with that starter cell's network. By running this algorithm for all starter cells that have at least one single-starter barcode, two connectivity datasets are generated: 1) a dataset with each row corresponding to a starter and aggregated information on its connections 2) a dataset outlining, for each connection, the CBCs and cell types of the starter and non-starter cells.

Network visualization and analysis

To visualize the outputs from connectivity inference, graph creation functions (`graph_draw()` and `graph_p1ot()`) were created to convert the datasets into directed graphs using the NetworkX package¹⁰⁴ in Python. Graphs were drawn using the following customizations: Neato layout using Graphviz¹⁰⁵ for node positioning, node size scaled by degree, nodes colored by cell type, edges with uniform thickness, and edges colored by the cell type of the non-starter cell.

954

955 **Analysis of cell type–specific connectivity enrichment**

956 To identify biases in observed cell type connectivity and how they differ from networks predicted by chance,
957 observed and null connectivity matrices were generated. By aggregating data from single-starter networks by
958 cell type, an observed adjacency matrix was calculated with rows and columns corresponding to the non-
959 starter and starter cell types, respectively. To generate the observed connectivity matrix, we divided the
960 number of connections observed between each pair of cell types (e.g. non-starter GABAergic to starter L2/3
961 ExNs) by the total number of connections observed. The null connectivity matrix was determined by the
962 relative abundance of cell types among our starter cell population (starter cell probabilities) and cell types in
963 our slice overall based on the uninfected population (non-starter cell probabilities). Starter cells were defined
964 as cells from all of the combined SAD B19 (n=7 datasets) and CVS-N2c (n=4 datasets) datasets described
965 above with ≥ 3 UMIs of helper virus transcripts detected. In addition, we generated a dataset in which the
966 helper virus expressed GFP and TVA but not G, and included all of the dTomato+ cells from this experiment as
967 starter cells for this analysis ([Table S3](#)). Non-starter probabilities were derived from the population of
968 uninfected cells. The null connectivity matrix was then generated by multiplying the proportion of each cell type
969 among non-starter cells in a pairwise manner by the proportion of each cell type among starter cells.
970 Enrichment scores were computed by dividing each observed probability by the corresponding null probability
971 and log₁₀ scaling the ratios to center them around 1, with negative values indicating the observed connection
972 was less likely than chance and positive values indicating the connection was more likely than chance. To
973 assess for statistically significant differences between the observed and null probabilities, the null distributions
974 for each connection were modeled using binomial distributions (n = total number of observed connections, p =
975 null probability of connection between two cell types) and two-sided binomial tests using the SciPy package in
976 Python with Bonferroni connections were performed. P-values less than .05 were considered significant.

977 **SUPPLEMENTAL INFORMATION**

978 Document S1. Figures S1-S8

979 Table S1. Barcode whitelist. Data from a recent publication¹¹, related to Figures 1 and S1

980 Table S2. Primers used for sequencing library generation, related to Figures 1, 2, 6, 7, and S1

981 Table S3. sc/snRNA-seq metadata, related to Figures 4, 5, 6, 7, 8 and S4, S5, S7, and S8

982 Table S4. Cell type-matched RVdG barcodes for connectivity analysis, related to Figures 8, S7, and S8

983

984

985

986 REFERENCES

- 987 1. Wickersham, I.R., Finke, S., Conzelmann, K.-K., and Callaway, E.M. (2007). Retrograde neuronal tracing
988 with a deletion-mutant rabies virus. *Nat. Methods* **4**, 47–49.
- 989 2. Miyamichi, K., Amat, F., Moussavi, F., Wang, C., Wickersham, I., Wall, N.R., Taniguchi, H., Tasic, B.,
990 Huang, Z.J., He, Z., et al. (2011). Cortical representations of olfactory input by trans-synaptic tracing.
991 *Nature* **472**, 191–196.
- 992 3. Clark, I.C., Gutiérrez-Vázquez, C., Wheeler, M.A., Li, Z., Rothhammer, V., Linnerbauer, M., Sanmarco,
993 L.M., Guo, L., Blain, M., Zandee, S.E.J., et al. (2021). Barcoded viral tracing of single-cell interactions in
994 central nervous system inflammation. *Science* **372**. <https://doi.org/10.1126/science.abf1230>.
- 995 4. Saunders, A., Huang, K.W., Vondrak, C., Hughes, C., Smolyar, K., Sen, H., Philson, A.C., Nemesh, J.,
996 Wysoker, A., Kashin, S., et al. (2022). Ascertaining cells' synaptic connections and RNA expression
997 simultaneously with barcoded rabies virus libraries. *Nat. Commun.* **13**, 6993.
- 998 5. Zhang, A., Jin, L., Yao, S., Matsuyama, M., van Velthoven, C., Sullivan, H., Sun, N., Kellis, M., Tasic, B.,
999 Wickersham, I.R., et al. (2024). Rabies virus-based barcoded neuroanatomy resolved by single-cell RNA
000 and in situ sequencing. *Elife*. <https://doi.org/10.7554/eLife.87866>.
- 001 6. Wickersham, I.R., Sullivan, H.A., and Seung, H.S. (2010). Production of glycoprotein-deleted rabies
002 viruses for monosynaptic tracing and high-level gene expression in neurons. *Nat. Protoc.* **5**, 595–606.
- 003 7. Finke, S., and Conzelmann, K.K. (1999). Virus promoters determine interference by defective RNAs:
004 selective amplification of mini-RNA vectors and rescue from cDNA by a 3' copy-back ambisense rabies
005 virus. *J. Virol.* **73**, 3818–3825.
- 006 8. Schnell, M.J., Mebatsion, T., and Conzelmann, K.K. (1994). Infectious rabies viruses from cloned cDNA.
007 *EMBO J.* **13**, 4195–4203.
- 008 9. Negri, A., and Foundation, C.S. (1905). *Contributo allo studio dell'eziologia della rabbia* (Tipografia e
009 Legatoria Cooperativa).
- 010 10. Lahaye, X., Vidy, A., Pomier, C., Obiang, L., Harper, F., Gaudin, Y., and Blondel, D. (2009). Functional
011 characterization of Negri bodies (NBs) in rabies virus-infected cells: Evidence that NBs are sites of viral
012 transcription and replication. *J. Virol.* **83**, 7948–7958.
- 013 11. Delgado, R.N., Allen, D.E., Keefe, M.G., Mancía Leon, W.R., Ziffra, R.S., Crouch, E.E., Alvarez-Buylla, A.,
014 and Nowakowski, T.J. (2022). Individual human cortical progenitors can produce excitatory and inhibitory
015 neurons. *Nature* **601**, 397–403.
- 016 12. Shannon, C.E. (1948). A mathematical theory of communication. *Bell Syst. Tech. J.* **27**, 379–423.
- 017 13. Adami, C. (2004). Information theory in molecular biology. *Phys. Life Rev.* **1**, 3–22.
- 018 14. Wickersham, I.R., and Sullivan, H.A. (2015). Rabies viral vectors for monosynaptic tracing and targeted
019 transgene expression in neurons. *Cold Spring Harb. Protoc.* **2015**, 375–385.
- 020 15. Osakada, F., and Callaway, E.M. (2013). Design and generation of recombinant rabies virus vectors. *Nat.*
021 *Protoc.* **8**, 1583–1601.
- 022 16. Ghanem, A., and Conzelmann, K.-K. (2016). G gene-deficient single-round rabies viruses for neuronal
023 circuit analysis. *Virus Res.* **216**, 41–54.

- 024 17. Sumser, A., Joesch, M., Jonas, P., and Ben-Simon, Y. (2022). Fast, high-throughput production of
025 improved rabies viral vectors for specific, efficient and versatile transsynaptic retrograde labeling. *Elife* 11.
026 <https://doi.org/10.7554/eLife.79848>.
- 027 18. Kim, E.J., Jacobs, M.W., Ito-Cole, T., and Callaway, E.M. (2016). Improved Monosynaptic Neural Circuit
028 Tracing Using Engineered Rabies Virus Glycoproteins. *Cell Rep.* 15, 692–699.
- 029 19. Ian Wickersham, Shenqin Yao, Bosiljka Tasic, Xiaoyin Chen (2024). Highly multiplexed circuit mapping
030 using barcoded rabies viruses and in situ sequencing.
- 031 20. Molliver, M.E., Kostović, I., and van der Loos, H. (1973). The development of synapses in cerebral cortex
032 of the human fetus. *Brain Res.* 50, 403–407.
- 033 21. Kostovic, I., and Rakic, P. (1990). Developmental history of the transient subplate zone in the visual and
034 somatosensory cortex of the macaque monkey and human brain. *J. Comp. Neurol.* 297, 441–470.
- 035 22. Korsunsky, I., Millard, N., Fan, J., Slowikowski, K., Zhang, F., Wei, K., Baglaenko, Y., Brenner, M., Loh,
036 P.-R., and Raychaudhuri, S. (2019). Fast, sensitive and accurate integration of single-cell data with
037 Harmony. *Nat. Methods* 16, 1289–1296.
- 038 23. Becht, E., McInnes, L., Healy, J., Dutertre, C.-A., Kwok, I.W.H., Ng, L.G., Ginhoux, F., and Newell, E.W.
039 (2018). Dimensionality reduction for visualizing single-cell data using UMAP. *Nat. Biotechnol.* 37, 38–44.
- 040 24. Blondel, V.D., Guillaume, J.-L., Lambiotte, R., and Lefebvre, E. (2008). Fast unfolding of communities in
041 large networks. *J. Stat. Mech.* 2008, P10008.
- 042 25. Joshi, P.S., Molyneaux, B.J., Feng, L., Xie, X., Macklis, J.D., and Gan, L. (2008). *Bhlhb5* regulates the
043 postmitotic acquisition of area identities in layers II–V of the developing neocortex. *Neuron* 60, 258–272.
- 044 26. Ozair, M.Z., Kirst, C., van den Berg, B.L., Ruzo, A., Rito, T., and Brivanlou, A.H. (2018). HPSC modeling
045 reveals that fate selection of cortical deep projection neurons occurs in the subplate. *Cell Stem Cell* 23,
046 60–73.e6.
- 047 27. Cubelos, B., Sebastián-Serrano, A., Beccari, L., Calcagnotto, M.E., Cisneros, E., Kim, S., Dopazo, A.,
048 Alvarez-Dolado, M., Redondo, J.M., Bovolenta, P., et al. (2010). *Cux1* and *Cux2* regulate dendritic
049 branching, spine morphology, and synapses of the upper layer neurons of the cortex. *Neuron* 66, 523–
050 535.
- 051 28. Weiss, L.A., and Nieto, M. (2019). The crux of *Cux* genes in neuronal function and plasticity. *Brain Res.*
052 1705, 32–42.
- 053 29. Fame, R.M., MacDonald, J.L., and Macklis, J.D. (2011). Development, specification, and diversity of
054 callosal projection neurons. *Trends Neurosci.* 34, 41–50.
- 055 30. Qian, X., Coleman, K., Jiang, S., Kriz, A.J., Marciano, J.H., Luo, C., Cai, C., Manam, M.D., Caglayan, E.,
056 Otani, A., et al. (2024). Spatial single-cell analysis decodes cortical layer and area specification. *bioRxiv.*
057 <https://doi.org/10.1101/2024.06.05.597673>.
- 058 31. Zeng, H., Shen, E.H., Hohmann, J.G., Oh, S.W., Bernard, A., Royall, J.J., Glattfelder, K.J., Sunkin, S.M.,
059 Morris, J.A., Guillozet-Bongaarts, A.L., et al. (2012). Large-scale cellular-resolution gene profiling in
060 human neocortex reveals species-specific molecular signatures. *Cell* 149, 483–496.
- 061 32. Clark, E.A., Rutlin, M., Capano, L.S., Aviles, S., Saadon, J.R., Taneja, P., Zhang, Q., Bullis, J.B., Lauer,
062 T., Myers, E., et al. (2020). Cortical *RORβ* is required for layer 4 transcriptional identity and barrel integrity.
063 *Elife* 9. <https://doi.org/10.7554/eLife.52370>.

- 064 33. Allen, T., and Lobe, C.G. (1999). A comparison of Notch, Hes and Grg expression during murine
065 embryonic and post-natal development. *Cell. Mol. Biol.* *45*, 687–708.
- 066 34. Molyneaux, B.J., Arlotta, P., Menezes, J.R.L., and Macklis, J.D. (2007). Neuronal subtype specification in
067 the cerebral cortex. *Nat. Rev. Neurosci.* *8*, 427–437.
- 068 35. Galazo, M.J., Emsley, J.G., and Macklis, J.D. (2016). Corticothalamic projection neuron development
069 beyond subtype specification: Fog2 and intersectional controls regulate intraclass neuronal diversity.
070 *Neuron* *91*, 90–106.
- 071 36. Galazo, M.J., Sweetser, D.A., and Macklis, J.D. (2023). Tle4 controls both developmental acquisition and
072 early post-natal maturation of corticothalamic projection neuron identity. *Cell Rep.* *42*, 112957.
- 073 37. Arlotta, P., Molyneaux, B.J., Chen, J., Inoue, J., Kominami, R., and Macklis, J.D. (2005). Neuronal
074 subtype-specific genes that control corticospinal motor neuron development in vivo. *Neuron* *45*, 207–221.
- 075 38. Trevino, A.E., Müller, F., Andersen, J., Sundaram, L., Kathiria, A., Shcherbina, A., Farh, K., Chang, H.Y.,
076 Paşca, A.M., Kundaje, A., et al. (2021). Chromatin and gene-regulatory dynamics of the developing
077 human cerebral cortex at single-cell resolution. *Cell* *184*, 5053–5069.e23.
- 078 39. Ziffra, R.S., Kim, C.N., Ross, J.M., Wilfert, A., Turner, T.N., Haeussler, M., Casella, A.M., Przytycki, P.F.,
079 Keough, K.C., Shin, D., et al. (2021). Single-cell epigenomics reveals mechanisms of human cortical
080 development. *Nature* *598*, 205–213.
- 081 40. Wang, Y., Dye, C.A., Sohal, V., Long, J.E., Estrada, R.C., Roztocil, T., Lufkin, T., Deisseroth, K., Baraban,
082 S.C., and Rubenstein, J.L.R. (2010). Dlx5 and Dlx6 regulate the development of parvalbumin-expressing
083 cortical interneurons. *J. Neurosci.* *30*, 5334–5345.
- 084 41. Cobos, I., Long, J.E., Thwin, M.T., and Rubenstein, J.L. (2006). Cellular patterns of transcription factor
085 expression in developing cortical interneurons. *Cereb. Cortex* *16 Suppl 1*, i82–i88.
- 086 42. Yao, Z., van Velthoven, C.T.J., Kunst, M., Zhang, M., McMillen, D., Lee, C., Jung, W., Goldy, J., Abdelhak,
087 A., Aitken, M., et al. (2023). A high-resolution transcriptomic and spatial atlas of cell types in the whole
088 mouse brain. *Nature* *624*, 317–332.
- 089 43. Pringle, N.P., and Richardson, W.D. (1993). A singularity of PDGF alpha-receptor expression in the
090 dorsoventral axis of the neural tube may define the origin of the oligodendrocyte lineage. *Development*
091 *117*, 525–533.
- 092 44. Pringle, N.P., Mudhar, H.S., Collarini, E.J., and Richardson, W.D. (1992). PDGF receptors in the rat CNS:
093 during late neurogenesis, PDGF alpha-receptor expression appears to be restricted to glial cells of the
094 oligodendrocyte lineage. *Development* *115*, 535–551.
- 095 45. Englund, C., Fink, A., Lau, C., Pham, D., Daza, R.A.M., Bulfone, A., Kowalczyk, T., and Hevner, R.F.
096 (2005). Pax6, Tbr2, and Tbr1 are expressed sequentially by radial glia, intermediate progenitor cells, and
097 postmitotic neurons in developing neocortex. *J. Neurosci.* *25*, 247–251.
- 098 46. Kawaguchi, A., Ikawa, T., Kasukawa, T., Ueda, H.R., Kurimoto, K., Saitou, M., and Matsuzaki, F. (2008).
099 Single-cell gene profiling defines differential progenitor subclasses in mammalian neurogenesis.
100 *Development* *135*, 3113–3124.
- 101 47. Hevner, R.F., Hodge, R.D., Daza, R.A.M., and Englund, C. (2006). Transcription factors in glutamatergic
102 neurogenesis: conserved programs in neocortex, cerebellum, and adult hippocampus. *Neurosci. Res.* *55*,
103 223–233.
- 104 48. Pollen, A.A., Nowakowski, T.J., Chen, J., Retallack, H., Sandoval-Espinosa, C., Nicholas, C.R., Shuga, J.,

- 105 Liu, S.J., Oldham, M.C., Diaz, A., et al. (2015). Molecular identity of human outer radial glia during cortical
106 development. *Cell* 163, 55–67.
- 107 49. Nakamura, Y., Sakakibara, S. i., Miyata, T., Ogawa, M., Shimazaki, T., Weiss, S., Kageyama, R., and
108 Okano, H. (2000). The bHLH gene *hes1* as a repressor of the neuronal commitment of CNS stem cells. *J.*
109 *Neurosci.* 20, 283–293.
- 110 50. Ohtsuka, T., Sakamoto, M., Guillemot, F., and Kageyama, R. (2001). Roles of the basic helix-loop-helix
111 genes *Hes1* and *Hes5* in expansion of neural stem cells of the developing brain. *J. Biol. Chem.* 276,
112 30467–30474.
- 113 51. Verkman, A.S., Binder, D.K., Bloch, O., Auguste, K., and Papadopoulos, M.C. (2006). Three distinct roles
114 of aquaporin-4 in brain function revealed by knockout mice. *Biochim. Biophys. Acta* 1758, 1085–1093.
- 115 52. Nagelhus, E.A., and Ottersen, O.P. (2013). Physiological roles of aquaporin-4 in brain. *Physiol. Rev.* 93,
116 1543–1562.
- 117 53. Yao, X., Derugin, N., Manley, G.T., and Verkman, A.S. (2015). Reduced brain edema and infarct volume
118 in aquaporin-4 deficient mice after transient focal cerebral ischemia. *Neurosci. Lett.* 584, 368–372.
- 119 54. Brenner, M., Kisseberth, W.C., Su, Y., Besnard, F., and Messing, A. (1994). GFAP promoter directs
120 astrocyte-specific expression in transgenic mice. *J. Neurosci.* 14, 1030–1037.
- 121 55. Holst, C.B., Brøchner, C.B., Vitting-Seerup, K., and Møllgård, K. (2019). Astroglialogenesis in human fetal
122 brain: complex spatiotemporal immunoreactivity patterns of GFAP, S100, AQP4 and YKL-40. *J. Anat.* 235,
123 590–615.
- 124 56. Su, M., Hu, H., Lee, Y., d’Azzo, A., Messing, A., and Brenner, M. (2004). Expression specificity of GFAP
125 transgenes. *Neurochem. Res.* 29, 2075–2093.
- 126 57. Gerdes, J., Schwab, U., Lemke, H., and Stein, H. (1983). Production of a mouse monoclonal antibody
127 reactive with a human nuclear antigen associated with cell proliferation. *Int. J. Cancer* 31, 13–20.
- 128 58. Reardon, T.R., Murray, A.J., Turi, G.F., Wirblich, C., Croce, K.R., Schnell, M.J., Jessell, T.M., and
129 Losonczy, A. (2016). Rabies virus CVS-N2c(Δ G) strain enhances retrograde synaptic transfer and
130 neuronal viability. *Neuron* 89, 711–724.
- 131 59. Kügler, S., Kilic, E., and Bähr, M. (2003). Human synapsin 1 gene promoter confers highly neuron-specific
132 long-term transgene expression from an adenoviral vector in the adult rat brain depending on the
133 transduced area. *Gene Ther.* 10, 337–347.
- 134 60. Marshel, J.H., Mori, T., Nielsen, K.J., and Callaway, E.M. (2010). Targeting single neuronal networks for
135 gene expression and cell labeling in vivo. *Neuron* 67, 562–574.
- 136 61. Beier, K.T. (2021). The Serendipity of Viral Trans-Neuronal Specificity: More Than Meets the Eye. *Front.*
137 *Cell. Neurosci.* 15, 720807.
- 138 62. Detje, C.N., Lienenklaus, S., Chhatbar, C., Spanier, J., Prajeeth, C.K., Soldner, C., Tovey, M.G., Schlüter,
139 D., Weiss, S., Stangel, M., et al. (2015). Upon intranasal vesicular stomatitis virus infection, astrocytes in
140 the olfactory bulb are important interferon Beta producers that protect from lethal encephalitis. *J. Virol.* 89,
141 2731–2738.
- 142 63. Pfefferkorn, C., Kallfass, C., Lienenklaus, S., Spanier, J., Kalinke, U., Rieder, M., Conzelmann, K.-K.,
143 Michiels, T., and Staeheli, P. (2015). Abortively infected astrocytes appear to represent the main source of
144 interferon beta in the virus-infected brain. *J. Virol.* 90, 2031–2038.

- 145 64. Drokhllyansky, E., Göz Aytürk, D., Soh, T.K., Chrenek, R., O'Loughlin, E., Madore, C., Butovsky, O., and
146 Cepko, C.L. (2017). The brain parenchyma has a type I interferon response that can limit virus spread.
147 *Proc. Natl. Acad. Sci. U. S. A.* *114*, E95–E104.
- 148 65. Bakken, T.E., Hodge, R.D., Miller, J.A., Yao, Z., Nguyen, T.N., Aebermann, B., Barkan, E., Bertagnolli, D.,
149 Casper, T., Dee, N., et al. (2018). Single-nucleus and single-cell transcriptomes compared in matched
150 cortical cell types. *PLoS One* *13*, e0209648.
- 151 66. Patiño, M., Lagos, W.N., Patne, N.S., Tasic, B., Zeng, H., and Callaway, E.M. (2022). Single-cell
152 transcriptomic classification of rabies-infected cortical neurons. *Proc. Natl. Acad. Sci. U. S. A.* *119*,
153 e2203677119.
- 154 67. Bernardi, A., and Spahr, P.F. (1972). Nucleotide sequence at the binding site for coat protein on RNA of
155 bacteriophage R17. *Proc. Natl. Acad. Sci. U. S. A.* *69*, 3033–3037.
- 156 68. Chubb, J.R., Trcek, T., Shenoy, S.M., and Singer, R.H. (2006). Transcriptional pulsing of a developmental
157 gene. *Curr. Biol.* *16*, 1018–1025.
- 158 69. Ostlund, C., Folker, E.S., Choi, J.C., Gomes, E.R., Gundersen, G.G., and Worman, H.J. (2009). Dynamics
159 and molecular interactions of linker of nucleoskeleton and cytoskeleton (LINC) complex proteins. *J. Cell*
160 *Sci.* *122*, 4099–4108.
- 161 70. Yang, S., Corbett, S.E., Koga, Y., Wang, Z., Johnson, W.E., Yajima, M., and Campbell, J.D. (2020).
162 Decontamination of ambient RNA in single-cell RNA-seq with DecontX. *Genome Biol.* *21*, 57.
- 163 71. Patiño, M., Rossa, M.A., Lagos, W.N., Patne, N.S., and Callaway, E.M. (2024). Transcriptomic cell-type
164 specificity of local cortical circuits. *Neuron* *0*. <https://doi.org/10.1016/j.neuron.2024.09.003>.
- 165 72. Kobschull, J.M., and Zador, A.M. (2018). Cellular barcoding: lineage tracing, screening and beyond. *Nat.*
166 *Methods* *15*, 871–879.
- 167 73. Lin, K.-Z., Li, L., Ma, W.-Y., Yang, X., Han, Z.-P., Luo, N.-S., Wang, J., and Xu, F.-Q. (2023). A rabies
168 virus-based toolkit for efficient retrograde labeling and monosynaptic tracing. *Neural Regeneration Res.*
169 *18*, 1827–1833.
- 170 74. Fus-Kujawa, A., Prus, P., Bajdak-Rusinek, K., Teper, P., Gawron, K., Kowalczyk, A., and Sieron, A.L.
171 (2021). An overview of methods and tools for transfection of eukaryotic cells in vitro. *Front. Bioeng.*
172 *Biotechnol.* *9*, 701031.
- 173 75. Miyamichi, K., Shlomai-Fuchs, Y., Shu, M., Weissbourd, B.C., Luo, L., and Mizrahi, A. (2013). Dissecting
174 local circuits: parvalbumin interneurons underlie broad feedback control of olfactory bulb output. *Neuron*
175 *80*, 1232–1245.
- 176 76. Kalidasan, V., Ng, W.H., Ishola, O.A., Ravichantar, N., Tan, J.J., and Das, K.T. (2021). A guide in lentiviral
177 vector production for hard-to-transfect cells, using cardiac-derived c-kit expressing cells as a model
178 system. *Sci. Rep.* *11*, 19265.
- 179 77. Lin, Z., Ophir, O., Trimbuch, T., Brokowski, B., Tibi, M., Pavletsov, P., Schmidt, H., Rosenmund, C.,
180 Hochgerner, H., and Zeisel, A. (2024). Brain-wide monosynaptic connectivity mapping with ROInet-seq.
181 *bioRxiv*, 2024.04.04.588058. <https://doi.org/10.1101/2024.04.04.588058>.
- 182 78. Kanold, P.O., Deng, R., and Meng, X. (2019). The integrative function of silent synapses on subplate
183 neurons in cortical development and dysfunction. *Front. Neuroanat.* *13*, 41.
- 184 79. Cancedda, L., Fiumelli, H., Chen, K., and Poo, M.-M. (2007). Excitatory GABA action is essential for
185 morphological maturation of cortical neurons in vivo. *J. Neurosci.* *27*, 5224–5235.

- 186 80. Wang, D.D., and Kriegstein, A.R. (2008). GABA regulates excitatory synapse formation in the neocortex
187 via NMDA receptor activation. *J. Neurosci.* 28, 5547–5558.
- 188 81. Ge, S., Goh, E.L.K., Sailor, K.A., Kitabatake, Y., Ming, G.-L., and Song, H. (2006). GABA regulates
189 synaptic integration of newly generated neurons in the adult brain. *Nature* 439, 589–593.
- 190 82. Kostović, I. (2020). The enigmatic fetal subplate compartment forms an early tangential cortical nexus and
191 provides the framework for construction of cortical connectivity. *Prog. Neurobiol.* 194, 101883.
- 192 83. Viswanathan, S., Bandyopadhyay, S., Kao, J.P.Y., and Kanold, P.O. (2012). Changing microcircuits in the
193 subplate of the developing cortex. *J. Neurosci.* 32, 1589–1601.
- 194 84. Viswanathan, S., Sheikh, A., Looger, L.L., and Kanold, P.O. (2017). Molecularly defined subplate neurons
195 project both to thalamocortical recipient layers and thalamus. *Cereb. Cortex* 27, 4759–4768.
- 196 85. Chen, T.-L., Deng, Q.-S., Lin, K.-Z., Zheng, X.-D., Wang, X., Zhong, Y.-W., Ning, X.-Y., Li, Y., Xu, F.-Q.,
197 Du, J.-L., et al. (2024). An applicable and efficient retrograde monosynaptic circuit mapping tool for larval
198 zebrafish. <https://doi.org/10.7554/elife.100880.1>.
- 199 86. Paranjape, N., Lin, Y.-H.T., Flores-Ramirez, Q., Sarin, V., Johnson, A.B., Chu, J., Paredes, M., and Wiita,
200 A.P. (2022). A CRISPR-engineered Isogenic Model Reveals Altered Neuronal Phenotypes of the 22q11.2
201 A-B Syndromic Deletion. *bioRxiv*, 2022.06.22.497212. <https://doi.org/10.1101/2022.06.22.497212>.
- 202 87. Chen, Y., Tristan, C.A., Chen, L., Jovanovic, V.M., Malley, C., Chu, P.-H., Ryu, S., Deng, T., Ormanoglu,
203 P., Tao, D., et al. (2021). A versatile polypharmacology platform promotes cytoprotection and viability of
204 human pluripotent and differentiated cells. *Nat. Methods* 18, 528–541.
- 205 88. Saxena, A., Wagatsuma, A., Noro, Y., Kuji, T., Asaka-Oba, A., Watahiki, A., Gurnot, C., Fagiolini, M.,
206 Hensch, T.K., and Carninci, P. (2012). Trehalose-enhanced isolation of neuronal sub-types from adult
207 mouse brain. *Biotechniques* 52, 381–385.
- 208 89. Habib, N., Avraham-Davidi, I., Basu, A., Burks, T., Shekhar, K., Hofree, M., Choudhury, S.R., Aguet, F.,
209 Gelfand, E., Ardlie, K., et al. (2017). Massively parallel single-nucleus RNA-seq with DroNc-seq. *Nat.*
210 *Methods* 14, 955–958.
- 211 90. Martelotto, L.G., Kalavros, N., Vlachos, I., and Wang, S. (2023). BIDMC TMC - low input single nuclei
212 sequencing isolation (NNLB).
- 213 91. Bushnell, B. (2022). BBMap. SourceForge. <https://sourceforge.net/projects/bbmap/>.
- 214 92. Smith, T., Heger, A., and Sudbery, I. (2017). UMI-tools: modeling sequencing errors in Unique Molecular
215 Identifiers to improve quantification accuracy. *Genome Res.* 27, 491–499.
- 216 93. Hunter, J.D. (2007). Matplotlib: A 2D Graphics Environment. *Comput. Sci. Eng.* 9, 90–95.
- 217 94. Harris, C.R., Millman, K.J., van der Walt, S.J., Gommers, R., Virtanen, P., Cournapeau, D., Wieser, E.,
218 Taylor, J., Berg, S., Smith, N.J., et al. (2020). Array programming with NumPy. *Nature* 585, 357–362.
- 219 95. The pandas development team (2020). Pandas (Zenodo) <https://doi.org/10.5281/zenodo.3509134>.
- 220 96. Waskom, M. (2021). seaborn: statistical data visualization. *J. Open Source Softw.* 6, 3021.
- 221 97. Hao, Y., Hao, S., Andersen-Nissen, E., Mauck, W.M., 3rd, Zheng, S., Butler, A., Lee, M.J., Wilk, A.J.,
222 Darby, C., Zager, M., et al. (2021). Integrated analysis of multimodal single-cell data. *Cell* 184, 3573–
223 3587.e29.

- 224 98. Korsunsky, I., Nathan, A., Millard, N., and Raychaudhuri, S. (2019). Presto scales Wilcoxon and auROC
225 analyses to millions of observations. *Bioinformatics*.
- 226 99. Blighe, K., Rana, S., Lewis, M. EnhancedVolcano: Publication-ready volcano plots with enhanced
227 colouring and labeling (Github).
- 228 100. Yu, G., Wang, L., Han, Y., and He, Q. (2012). "clusterProfiler: an R package for comparing biological
229 themes among gene clusters. *OMICS* 16, 284–287.
- 230 101. Wu, T., Hu, E., Xu, S., Chen, M., Guo, P., Dai, Z., Feng, T., Zhou, L., Tang, W., Zhan, L., et al. (2021).
231 clusterProfiler 4.0: A universal enrichment tool for interpreting omics data. *Innovation (Camb)* 2, 100141.
- 232 102. Andreatta, M., and Carmona, S.J. (2021). UCell: Robust and scalable single-cell gene signature scoring.
233 *Comput. Struct. Biotechnol. J.* 19, 3796–3798.
- 234 103. Virtanen, P., Gommers, R., Oliphant, T.E., Haberland, M., Reddy, T., Cournapeau, D., Burovski, E.,
235 Peterson, P., Weckesser, W., Bright, J., et al. (2020). SciPy 1.0: fundamental algorithms for scientific
236 computing in Python. *Nat. Methods* 17, 261–272.
- 237 104. Aric, A., Hagberg, D.A., and Schult, P.J. (2008). Exploring network structure, dynamics, and function using
238 NetworkX". In *Proceedings of the 7th Python in Science Conference (SciPy2008)*, Gael Varoquaux, T.
239 Vaught and J. Millman, eds., pp. 11–15.
- 240 105. Gansner, E.R., and North, S.C. (2000). An open graph visualization system and its applications to
241 software engineering. *Softw. Pract. Exp.* 30, 1203–1233.
- 242